Master Thesis in Geographical Information Science nr 143

Mapping Fire Salamander (*Salamandra salamandra*) Habitat Suitability in Baden-Württemberg with Multi-Temporal Sentinel-1 and Sentinel-2 Imagery

Andreas Eriksson

2022
Department of
Physical Geography and Ecosystem Science
Centre for Geographical Information Systems
Lund University
Sölvegatan 12
S-223 62 Lund
Sweden

Andreas Eriksson (2022). “Mapping Fire Salamander (*Salamandra salamandra*) Habitat Suitability in Baden-Württemberg with Multi-Temporal Sentinel-1 and Sentinel-2 Imagery”. Master degree thesis, 30 credits in Master in Geographical Information Science. Department of Physical Geography and Ecosystem Science, Lund University.

Mapping Fire Salamander (*Salamandra salamandra*) Habitat Suitability in Baden-Württemberg with Multi-Temporal Sentinel-1 and Sentinel-2 Imagery

---

Andreas Eriksson
Master Thesis in Geographical Information Science

Supervised by:

Anders Ahlström
Department of Physical Geography and Ecosystem Science
Lund University, Sweden

Johannes Penner
Chair of Wildlife Ecology and Management
University of Freiburg, Germany

Abstract

Remote sensing image classification is used in land cover, forest type and tree species classifications but rarely considered for habitat suitability modelling of animal and plant species. It is instead common that land cover products derived from remote sensing data are used in these modelling problems, even though satellite imagery can provide more detailed information. The aim of this project was thus to explore remote sensing image classification methods to classify land covers in Baden-Württemberg based on their habitat suitability for the fire salamander (*Salamandra salamandra*). Fire salamanders depend on both suitable aquatic and terrestrial environments, and the classification was therefore applied on multi-temporal Sentinel-1 and Sentinel-2 images combined with a waterway proximity layer derived from OpenStreetMap data. The classification used a random forest classifier which was trained to discriminate between positive samples from tree covered areas within 300 m of fire salamander observations and unlabelled samples drawn from a regular grid with 1500 m point spacing in the study area. Two classification methods were evaluated: pixel-based, in which single pixels are used in the classification, and superpixel-based, in which the classification was performed on mean pixel values of approximately equally sized (∼1 ha) vectorized regions of similar pixels derived from a Simple Linear Iterative Clustering (SLIC) segmentation of the study area. The resultant classifications were compared against a model with land cover data from Copernicus Land Monitoring Service, and the evaluation showed that the image classifications were able to discriminate better between positive and unlabelled test samples. The superpixel-based classification further achieved a higher evaluation score (AUC: 0.91) than the pixel-based classification (AUC: 0.90), and was thus the best model in the analysis. An exploratory analysis of the predictions based on LUCAS 2018 survey points further indicated that the models predicted high fire salamander habitat suitability in tree covered areas situated within roughly 200 m of stream and river features, with more than 10 % canopy cover, and with more than 25 % of broadleaved trees in the canopy composition. Remote sensing image classification for fire salamander habitat suitability modelling was concluded applicable at regional mapping scales, and more generally for habitat suitability modelling of species that are highly dependent on land cover characteristics.

Contents

List of Abbreviations

AUC Area Under the ROC Curve

DEM Digital Elevation Model

GLCM Grey-Level Co-Occurrence Matrix

GRD Ground Range Detected

IDAN Intensity-Driven Adaptive-Neighbourhood (speckle filter)

IW Interferometric Wide

LUCAS Land Use and Coverage Area frame Survey

NDVI Normalized Difference Vegetation Index

NDWI Normalized Difference Water Index

NIR Near Infra-Red

PU-learning Positive-Unlabelled learning

RANSAC Random Sample Consensus

RMSE Root Mean Square Error

ROC Receiver Operating Characteristic (curve)

SAR Synthetic Aperture Radar

SDM Species Distribution Modelling

SLIC Simple Linear Iterative Clustering

SRTM Shuttle Radar Topography Mission

SWIR Short-Wave Infra-Red

List of Figures

List of Tables

1 Introduction

A global decline in amphibian populations has been noticed for more than 30 years (Green et al. 2020). Habitat loss due to human activities and a continued spread of the amphibian skin disease chytridiomycosis are important drivers of this decline (Blaustein and Kiesecker 2002; Scheele et al. 2019). Chytridiomycosis is known to be caused by the fungi: *Batrachochytrium dendrobatidis* (*Bd*) and *Batrachochytrium salamandrivorans* (*Bsal*), and the latter is highly problematic for the fire salamander (*Salamandra salamandra*) in Europe (Martel, Sluijs, et al. 2013; Martel, Blooi, et al. 2014). Fire salamanders show no immune response to *Bsal* infection which is lethal to most individuals, and rapid population declines have therefore been noticed in affected populations (Stegen et al. 2017). *Bsal* has since it was discovered in the Netherlands, also been detected in Belgium, Germany, and Spain (Martel, Vila-Escale, et al. 2020; Spitzen-van der Sluijs et al. 2016), and has further been termed the "salamander plague" (Stokstad 2014). Most *Bsal* cases have been recorded in western Germany, which is considered the current hotspot of the disease (Lötters et al. 2020). However, a continued spread is expected as models suggest that additional regions in Central Europe that are currently free from *Bsal* provide a suitable environment for the disease (Beukema, Martel, et al. 2018; Beukema, Erens, et al. 2021; Lötters et al. 2020).

Fire salamander habitat suitability models can aid conservation programmes of the species since resultant distribution maps can be used in *Bsal* risk analyses to evaluate potential spread of the disease, or to identify areas with risk of habitat loss. These models are usually built with correlative species distribution modelling (SDM) methods by relating presence observations with environmental predictors that constrain the distribution of the species. Common predictors used in fire salamander SDM studies describe climatic conditions, topography, and land cover characteristics (e.g. see: Bani et al. 2015; Romero et al. 2012; Werner et al. 2013). However, climatic conditions are not necessarily useful at regional mapping scales since fire salamanders are found throughout a relatively large distribution range in Europe (see Figure 1.2) and thus show an adaptability to different climatic variations. Fire salamanders show great subspecies variation within the Iberian Peninsula, but, the high genetic similarity found outside the Iberian

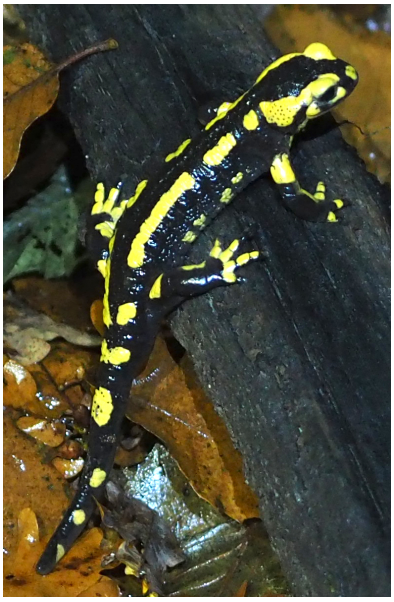

Figure 1.1: Adult fire salamander. Photo by Mélissa Msalmi in Bougival, France, 2021-10-30.

Peninsula (Burgon et al. 2021) suggests that these populations have a relatively large adaptability to different climatic conditions. The fire salamander is further a forest living species (Dufresnes 2019), and available climate data sets are generally unrepresentative of the climatic variations experienced below a forest canopy, where smaller temperature variations and more moist conditions can provide suitable habitats to amphibians (Escoriza and Hernandez 2021). Approaches to model the microclimate in forest from combinations of *in situ* measurements, weather station, and remote sensing data have been proposed (Lembrechts et al. 2019). However, *in situ* measurements are impractical for models over large heterogeneous regions, and the accuracy of the resultant microclimate model must be taken into consideration in the modelling.

Fire salamander habitat suitability models can thus be assumed to be highly dependent on land cover characteristics at regional mapping scales, which means that availability of suitable terrestrial and aquatic habitats must be accounted for. The aquatic habitat is used during the larval life stage of the species and usually consist of fish-free headwater streams (Thiesmeier and Schuhmacher 1990), although, small ponds or ditches (Antzen and Belkom 2020; Burgstaller et al. 2021; Steinfartz et al. 2007) and subterranean water bodies (Manenti et al. 2017) are also known to be used by the fire salamander. Larval development in the aquatic habitat depends on water temperature and food availability (Weitere et al. 2004), and metamorphosis typically occur after about three to five months in German

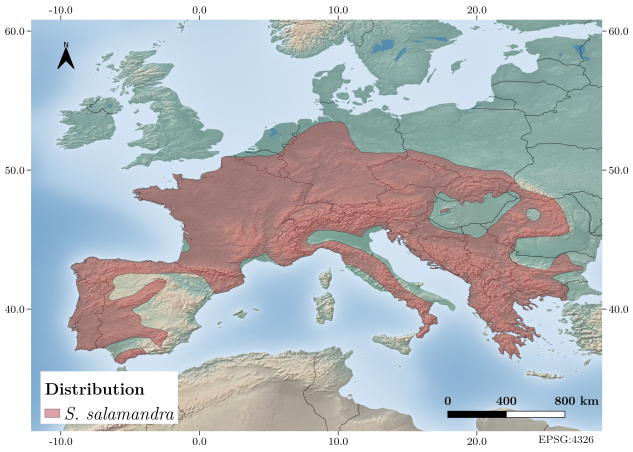

Figure 1.2: Fire salamander distribution from IUCN (International Union for Conservation of Nature), Conservation International & NatureServe (2009). "Salamandra salamandra". In: *The IUCN Red List of Threatened Species. Version 2021-1.* URL: https://www.iucnredlist.org.

populations (Thiesmeier and Schuhmacher 1990). Adult individuals thereafter live completely terrestrial lives (Steinfartz et al. 2007), however, the aquatic habitat must still be available for larval deposition. Forests, are the main terrestrial environment used by the species as previously mentioned, and Wagner et al. (2020) found broadleaved forests to have higher larval abundance than coniferous forests in western Germany.

Populations of the species thus rely on both terrestrial and aquatic environments which in addition must co-occur since fire salamanders typically remain within a limited extent. The full dispersal ability of the species is not yet fully investigated, but capture-recapture studies have indicated that most fire salamander movements are of distances shorter than 500 m (Ficetola et al. 2012). Estimates of average home range sizes, representing the mean area recaptured individuals moved within during the length of the study period, vary between studies, e.g. Burgstaller et al. (2021) found a mean home range size of 263 m^2, while Hendrix et al. (2017) reported 3894 m^2. These estimates are dependent on the size of the study area (Burgstaller et al. 2021), and the studies are further affected by the weather dependent activity of adult fire salamander (Catenazzi 2016) which makes the species difficult to monitor. Movement and home range estimates are therefore not fully representative of movements made by the studied individuals, however, these studies nevertheless provide knowledge regarding extents and distances in which movements can be expected.

Land cover predictors describing the availability of suitable terrestrial and

aquatic environments in habitat suitability models are often based on variables derived from land cover classification maps, however, these predictors have certain limitations. Land cover classifications partition the landscape into different information classes which for forest areas typically concern classes of coniferous, broadleaved, and possibly mixed forest types. No information of within class variation, e.g. proportion of broadleaved and coniferous trees within an area classified as mixed forest, is thus available during the modelling. Land cover classifications are on the other hand usually derived from high resolution remote sensing data sets which also is used in more forest specific applications such as: tree species classification (Persson et al. 2018), forest above ground biomass (Laurin et al. 2018), and canopy cover (Korhonen et al. 2017). It is therefore clear that these data sets have the potential to provide more information in habitat suitability modelling problems than what data from land cover classification maps provide.

This project therefore aims to investigate whether image classification techniques commonly used in e.g. land cover and tree species classifications, can be applied on high resolution remote sensing data sets to classify land covers based on their suitability as fire salamander habitats. This is similar to how SDMs are modelled, although, the predictor variables used are measures of physical properties and do not directly offer simple ecological interpretations. Remote sensing based habitat suitability models usually includes an intermediate processing step in which ecologically meaningful land cover predictors are derived from the remote sensing imagery (He et al. 2015). An image classification approach aim to identify suitable habitats directly from the remote sensing imagery, and thus remove the intermediate processing step of generating ecologically meaningful predictors, as visualised in Figure 1.3.

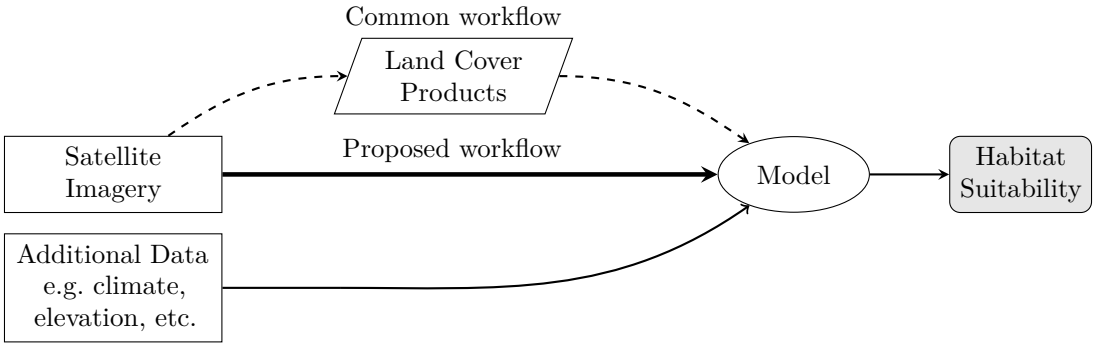

Figure 1.3: This project explore the usage of high resolution satellite images in habitat suitability modelling, which avoid the intermediate step of generating derived land cover products.

The habitat suitability study is performed in Baden-Württemberg in southwestern Germany for which a point set of fire salamander observations are available. *Bsal* has not yet been detected in Baden-Württemberg, but, records from neigh-

bouring Bavaria (Schmeller et al. 2020; Thein et al. 2020) highlight the need to prepare for a continued spread of the disease into Baden-Württemberg. Imagery from the Sentinel-1 and Sentinel-2 missions of European Union's Copernicus programme has been selected for the classification. These missions provide high resolution radar and optical products suitable for land monitoring with an open data policy. Using Sentinel-1 and Sentinel-2 data offer the possibility to classify habitat suitability at resolutions higher than the expected home range size of the fire salamander, and the usage of a superpixel-based image classification method, in which the classification is performed on approximately equally sized regions of similar and connected pixels, is therefore tested and compared against a pixel-based approach. Both methods are further contrasted against a model based on land cover classification data from Copernicus Land Monitoring Service. Apart from generating and comparing resultant fire salamander habitat suitability maps, the project aims to provide more knowledge regarding benefits and drawbacks with an image classification based approach compared to models derived with land cover classification data. An exploratory analysis of the model predictions is also applied in order to evaluate the most important habitat type for the fire salamander in Baden-Württemberg.

2 Methods

2.1 Study Site and Fire Salamander Observations

Baden-Württemberg is German state situated in southwestern Germany (49°0′ N, 9°0′ E). It covers an approximate 35 800 km^2, and is mainly composed of agricultural (∼50 %), forest and semi-natural (∼40 %), and artificial (∼10 %) land covers. The area has a varied topography and contain mountain ranges such as the Black Forest and the Swabian Alps, with the highest peak (Feldberg) reaching 1493 m above sea level. Figure 2.1 display an overview map of Baden-Württemberg, and shows the main land cover classes from the *CORINE Land Cover 2018* inventory provided by the Copernicus Land Monitoring Service.

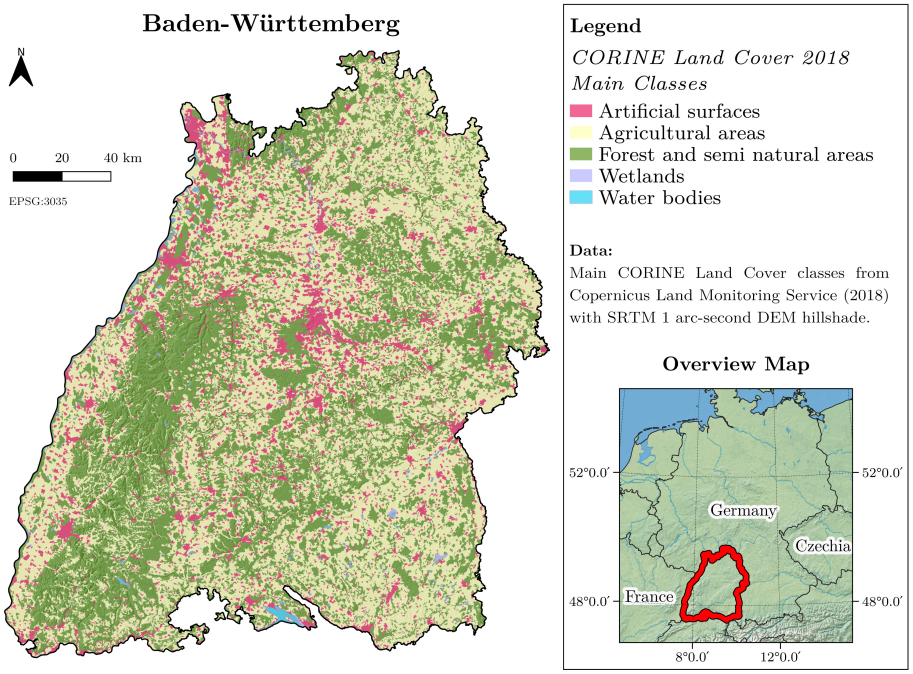

Figure 2.1: Map of Baden-Württemberg with the main classes of CORINE Land Cover 2018.

Fire salamander observations ($n = 2896$) from 2014 to 2021 were provided by Landesanstalt für Umwelt Baden-Württemberg (LUBW) for the study. The observations originate from two different monitoring projects open for public participation: "Landesweite Artenkartierung" (LUBW 2022b), and "Meldeplattformen" (LUBW 2022a). Although the former project is based on an organized sampling scheme with 5 km × 5 km grid cells which participants survey, no information regarding the sampling effort within each cell was known, and observations from both projects were therefore treated as opportunistic, i.e. not systematically collected. 15 recordings from 2014 to 2017 located within 500 m of areas with loss in tree cover in the *Tree Cover Change Mask 2015-2018* product from Copernicus Land Monitoring Service was removed from the point set since these observations possibly depend on land covers not available in 2018 and 2019, which was the temporal range considered in the modelling. Distribution of the filtered point observations in the study area can be seen in Figure 2.2.

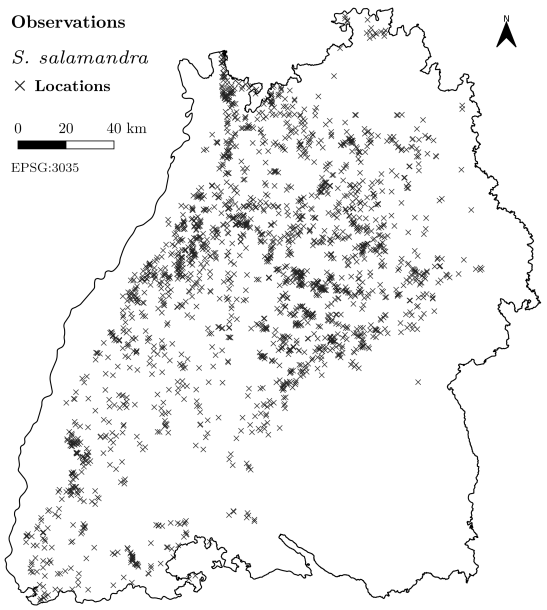

Figure 2.2: Distribution of filtered fire salamander observations in Baden-Württemberg used in the study.

2.2 Sentinel Data

The image classifications were performed with Sentinel-1 Level-1 Ground Range Detected (GRD) images acquired in Interferometric Wide (IW) swath mode and

Sentinel-2 Level-1C products from European Union's Copernicus programme. For Sentinel-1, IW swath mode is the main acquisition mode for land monitoring in which the C-band Synthetic Aperture Radar (SAR) instrument acquire dual polarisation (VV: vertical transmit – vertical receive, and VH: vertical transmit – horizontal receive) data at 5 m × 20 m spatial resolution. The Level-1 GRD products contain detected and multi-looked (an operation which averages the signal to reduce speckle noise) backscattered signal strength projected to ground range with a 10 m × 10 m pixel spacing (ESA 2021). The Sentinel-2 satellites are equipped with multi-spectral push broom sensors which acquire high-resolution optical imagery over four spectral bands in 10 m and six bands in 20 m spatial resolution. (The sensors also acquire three additional 60 m bands, but these were only used for atmospheric corrections.) Products in Level-1C processing level are orthorectified images in top of atmosphere reflectance.

The imagery was downloaded through the French *PEPS – Operating platform Sentinel products* portal at: https://peps.cnes.fr. Sentinel-1 images acquired in descending orbit direction was used since the full study area was covered within the swath width of a single descending orbit. Using images acquired in ascending orbit direction would have required mosaicking of images from two orbits (which implies two different acquisition dates), and was therefore avoided in the study. It was however necessary to use Sentinel-2 images from two orbits: relative orbit number 65 and 108 (hereafter simply referred to as orbit 65 and orbit 108), to cover the full study area. Combining the data over the two orbits was later performed with decision level fusion of models trained in overlapping areas as explained in Section 2.10. For each Sentinel-2 orbit, images from three acquisition dates with no or very low amount of visible cloud cover over the study area and at different parts of the 2018 and 2019 growing seasons were identified for download. Note that 2018 and 2019 falls within the temporal range of the fire salamander observations which are further described in Section 2.8. Sentinel-1 scenes was then selected at different periods over the corresponding growing seasons. No consideration of cloud cover is necessary in selection of Sentinel-1 scenes, since the C-band SAR instrument is an active sensor that can acquire images independent of weather or sunlight. Both the Sentinel-1 and Sentinel-2 products required several image tiles for each acquisition date to cover the study area and Table 2.1 provides an overview of all scenes downloaded for the classification.

Table 2.1: Sentinel-1 GRD and Sentinel-2 Level-1C images downloaded for the classifications. Each acquisition date used required several tiles to generate a full scene for the study area.

Orbit*	Direction	Acquisition Date	Platform	Product	No. Tiles
66	Desc.	2018 October 7	Sentinel-1B	IW Level-1 GRD	3
66	Desc.	2019 May 11	Sentinel-1B	IW Level-1 GRD	3
66	Desc.	2019 August 3	Sentinel-1B	IW Level-1 GRD	3
65	Desc.	2018 April 7	Sentinel-2B	Level-1C	8
65	Desc.	2018 April 27	Sentinel-2B	Level-1C	8
65	Desc.	2018 October 14	Sentinel-2B	Level-1C	8
108	Desc.	2018 September 27	Sentinel-2B	Level-1C	9
108	Desc.	2019 April 20	Sentinel-2A	Level-1C	9
108	Desc.	2019 June 29	Sentinel-2A	Level-1C	9

*Relative orbit number.

2.3 Sentinel-1 Processing

The downloaded Sentinel-1 Level-1 GRD images were processed in SNAP (*ESA SNAP* 2021) to obtain terrain-flattened γ^0 backscatter coefficients in both polarisations (VV and VH), following the workflow presented in Figure 2.3. The terrain-flattened γ^0 coefficient is a measure of the backscattered signal per area corrected for the local topography (Small 2011), which makes it suitable for usage in study areas with varying topography. This processing workflow began with common Sentinel-1 processing steps in which the satellite orbit information first was updated with a more accurate post-processed orbit file from the Copernicus Precise Orbit Determination Service, followed by thermal and border noise removal operations to reduce these noise signals in the pixels. Calibration to the β^0 backscatter coefficient was thereafter performed, and since the Sentinel-1 swaths are sliced into multiple tiles, it was also necessary to combine them into full scenes with the slice assembly tool in SNAP.

SAR images are affected by speckle noise (see Figure 2.4) and the Intensity-Driven Adaptive-Neighbourhood (IDAN) speckle filter (Vasile et al. 2006) was applied to limit its influence on the classification. The IDAN filter applies a region growing algorithm of the neighbourhood around a pixel, and the despeckled pixel value is thereafter estimated based on the mean and variance of the pixel values within the region (Vasile et al. 2006). The variance in the region determine the amount of smoothing applied, high variance in a region reduce the amount of smoothing and the resultant pixel value is set close to its original value, low region variance result in high smoothing and the new pixel value is set close to the mean value of the region. The filter was applied using an adaptive neighbourhood size

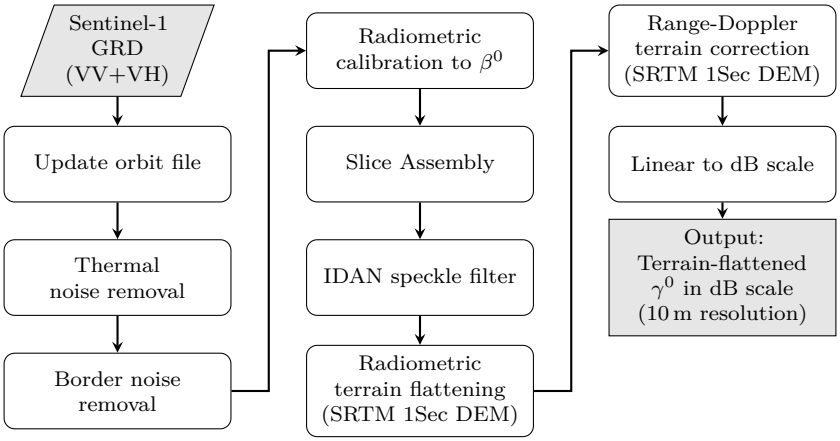

Figure 2.3: Sentinel-1 processing workflow applied in SNAP.

of 50 pixels and with the number of looks parameter set to one. The reciprocal square root of the number of looks parameter is a noise variation coefficient used as a threshold for inclusion/exclusion of pixels in the region growing algorithm. It thus controls the filtering since a smaller noise variation coefficient (which means that less speckle is expected in the image) results in less pixels included during the region growing process. Setting this parameter to one results in relatively large regions, and the choice was based on visual comparison between different parameter settings. An example of the speckle filtering is presented in Figure 2.4.

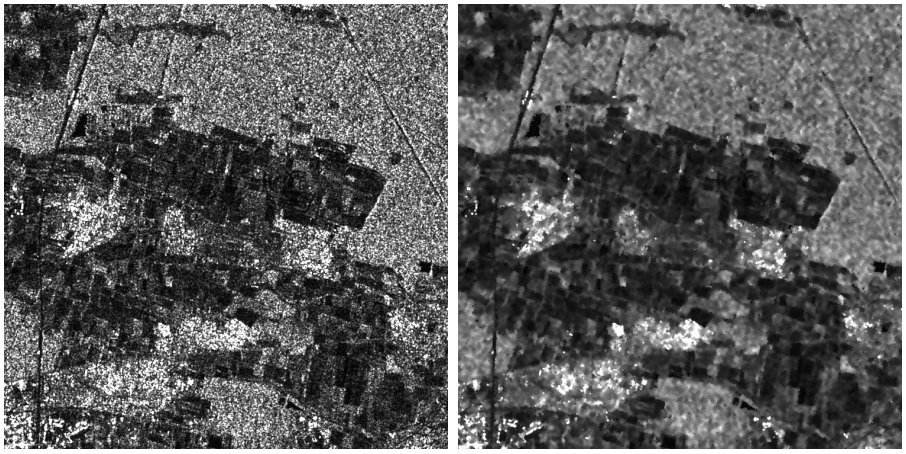

(a) Before speckle filtering. **(b)** After speckle filtering.

Figure 2.4: β_0 backscatter coefficient of *2019 May 11* scene subset in VH polarisation before (a) and after (b) IDAN speckle filtering.

The terrain-flattened γ^0 backscatter coefficient was then computed with the terrain flattening tool using the 1 arc-second Digital Elevation Model (DEM) from

the Shuttle Radar Topography Mission (SRTM) downloaded within SNAP. The result was orthorectified to 10 m resolution using Range-Doppler Terrain Correction, again with the SRTM DEM, and finally converted from linear to decibel (dB) scale.

2.4 Sentinel-2 Processing

The Sentinel-2 scenes were processed to derive a multi-temporal set of 10 m and 20 m spectral bands in bottom of atmosphere reflectance, and additional vegetation indices and texture metrics features further discussed in Section 2.5. An overview of the processing workflow is presented in Figure 2.5. First, atmospheric and terrain correction of all Sentinel-2 Level-1C image tiles to bottom of atmosphere reflectance (i.e. Level-2A products) was performed with Sen2Cor version 2.9 (MPC 2020). Similar settings as defined in issue 41 of the Level-2A Data Quality Report (MPC 2021, Section 3.1.1) was applied, including the auxiliary European Space Agency's Climate Change Initiative Land Cover data used to aid scene classification in the correction. The only difference in processing settings compared to the Level-2A Data Quality Report was that only 10 m and 20 m resolution layers were kept as outputs, and that the SRTM DEM was used in the correction. Note that this version of Sen2Cor failed to use the SRTM DEM in regions covering more than one DEM tile due to a known bug (see: https://forum.step.esa.int/t/processing-error-due-to-srtm-data-conflict/29796/6). This bug was caused by an error during the removal of a temporary DEM file open in a different process, and the suggested temporary bug fix: disable the temporary DEM file removal in "L2A_Tables.py", was applied such that all scenes could be processed consistently.

GDAL (GDAL/OGR contributors 2021) was thereafter used to mosaic the resultant tiles of corresponding dates, and the scenes were then visually inspected using the scene classification and true colour image outputs from Sen2Cor. No cloud cover was noticed in most of the scenes although certain agricultural and urban areas contained pixels misclassified with high cloud probability. The exception was two scenes in orbit 65: *2018 April 27* and *2018 October 10*, in which some cloud cover was found near the border of the study area. These areas were simply masked in all orbit 65 scenes since they were located within the zone of orbit overlap. A few scenes also contained areas classified as thin cirrus (i.e. cloud with high transparency), but, no additional treatment of these regions was performed. Figure 2.6 shows the final coverage of each orbit after removal of cloud covered areas.

The geolocation accuracy of Sentinel-2 scenes can result in co-registration errors between multi-temporal images that exceeds 10 m (Rufin et al. 2021). An additional co-registration of the Sentinel-2 scenes was therefore applied in order to correct for this disagreement, which can be visualized in Figure 2.7. No co-

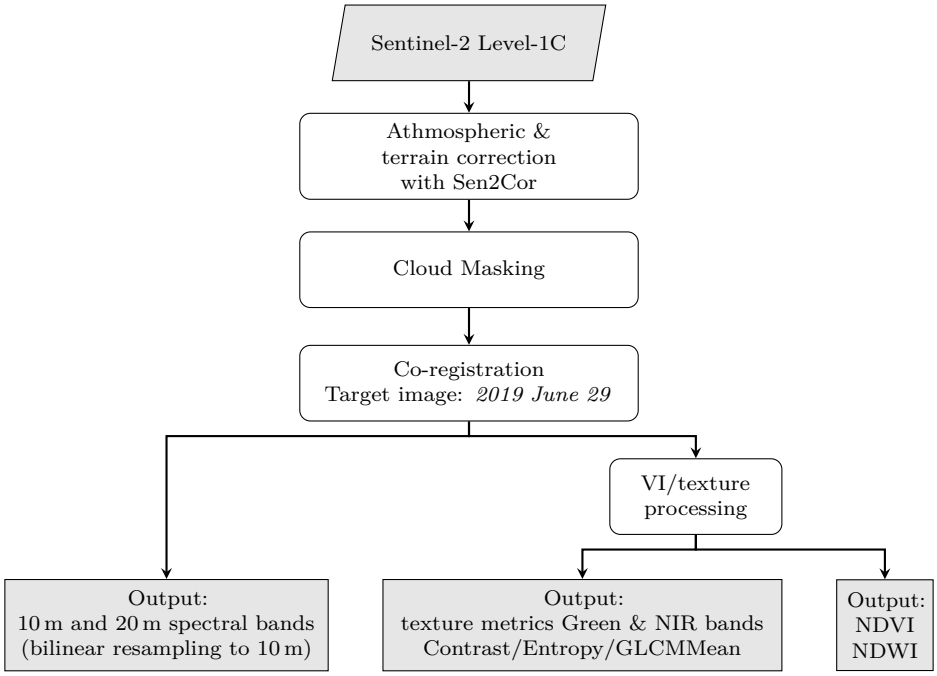

Figure 2.5: The processing workflow used to generate Sentinel-2 features for the classification.

registration of Sentinel-1 images was performed since the geolocation accuracy of the Sentinel-1 GRD products (3σ deviation of 7 m specified in CLS 2016) was considered sufficient for a multi-temporal analysis. The co-registration used the *2019 June 29* scene from orbit 108 as "target" image which all other "moving" images were co-registered against. A set of tie-points between the target image and the moving images were generated automatically using the phase correlation approach used in Skakun et al. (2017). Points were generated in a 1500 m × 1500 m grid throughout the target image, resulting in a total of 13 747 points of which 10 553 were located in the region of orbit overlap. Phase correlation derived image translation was then computed on the 10 m Near Infra-Red (NIR) bands using windows of 65 × 65 pixels centred over each grid point, such that each tie-point was assigned estimated local translation parameters. The phase correlation was computed with scikit-image (Walt et al. 2014) using an up-sampling factor of 100 which allow the algorithm to report detected translations at decimetre levels. The point set was then filtered by removal of points with unlikely large shifts ($\geq$30 m), and 1000 points were additionally set aside as test points used to evaluate the co-registration performance.

An affine transformation was used to transform the moving images in the co-registration. The transformation parameters were derived with Random Sample

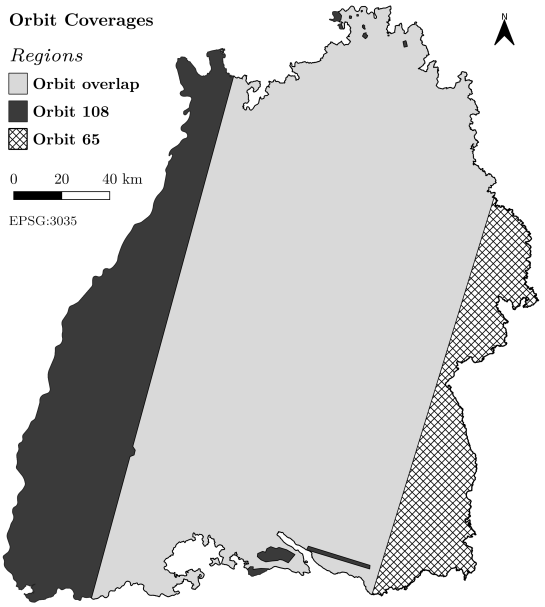

Figure 2.6: Sentinel-2 orbit coverages after cloud removal.

Consensus – RANSAC (Fischler and Bolles 1981) least squares regression in scikit-learn (Pedregosa et al. 2011). RANSAC regression is used to handle corrupt observations by an outlier detection algorithm in which models fitted to minimum sized subsets of the observations are used to classify observations as outliers or inliers (Fischler and Bolles 1981). The minimum subset size was set to three tie-points, which is the least amount of points needed to solve for the six transform parameters. Transformation parameters for the 20 m bands were derived directly from the 10 m transformations, and all images were assigned the modelled transformations by updating the image geotransform parameters with GDAL followed by bilinear resampling to 10 m resolution. Table 2.2 presents the number of inliers used in the model fitting and RMSE (Root Mean Square Error of coordinate differences) calculated on the test set before and after co-registration. Note that the test set was not filtered with RANSAC and may thus also contain outliers.

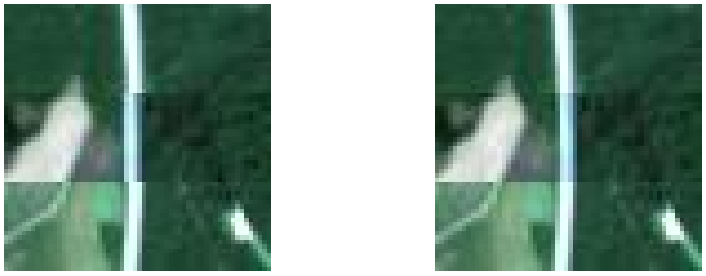

(a) Before co-registration. **(b)** After co-registration.

Figure 2.7: Image mosaics with the *2019 June 29* (top and bottom) and the *2018 September 27* (mid section) scenes before (a) and after (b) co-registration. The co-registration transform the moving image in the mid section of the mosaic to the target image which aligns the linear feature visible in the centre of the mosaics.

Table 2.2: Evaluation statistics from the co-registration of moving images to the target image *2019 June 29*.

		Test RMSE (m)	
Moving Image	No. Inliers	Before Co-Reg.	After Co-Reg.
2018 April 7	6824	7.5	5.2
2018 April 27	7701	4.1	2.1
2018 October 14	8004	7.1	4.4
2018 September 27	11 006	7.7	2.8
2019 April 20	9206	7.7	3.4

2.5 Vegetation Indices and Texture Features

Vegetation indices, designed to enhance vegetation characteristics in the images, were included in the classification since they potentially can improve a fire salamander habitat classification (e.g. Immitzer et al. (2019) found vegetation indices to improve the tree species classification in Central Europe). Indices based on normalized differences between two bands can in addition reduce the influence of topographic effects or shadows affecting both bands. A great amount of vegetation indices have been developed for different studies (see: https://www.indexdatabase.de/), but, only: the Normalized Difference Vegetation Index (NDVI; Rouse et al. 1974), and the Normalized Difference Water Index (NDWI; Gao 1996), were considered in this analysis. NDVI exploits the high reflectance in the NIR band and low reflectance in the Red band of live vegetation, and is calculated as a difference between the

bands normalized by their sum:

$$NDVI = \frac{NIR - Red}{NIR + Red}.$$

NDWI was developed to measure leaf water content, and use that dry vegetation have higher reflectance in the Short Wave Infra-Red (SWIR) band than green vegetation (Gao 1996). The NDWI index is calculated as a normalized difference between the NIR and SWIR bands:

$$NDWI = \frac{NIR - SWIR}{NIR + SWIR}.$$

NDVI and NDWI was calculated for all Sentinel-2 scenes using the 10 m Red and NIR bands, and the 20 m (Band 11) SWIR band.

Texture features, which provide information about the spatial variation in pixel values within a neighbourhood, was tested in the project since it was found to improve the old-growth forests classification in B. D. Spracklen and D. V. Spracklen (2019). Several texture metrics can be derived from the Grey-Level Co-Occurrence Matrix (GLCM) which contain count frequencies (normalized to probabilities with probabilistic quantizer) of how often two pixel values occur at a given displacement within a neighbourhood (Haralick et al. 1973). The metrics: Contrast, Entropy, and GLCM mean were considered for this analysis based on the recommendations in Hall-Beyer (2017). Contrast increases with larger differences between neighbouring pixels (assuming one pixel displacement), Entropy is a measure of disorder and depends on the amount of variation in pixel values between neighbouring pixels, and GLCM Mean is a weighted average of pixel values in the neighbourhood in which weights are taken from the GLCM matrix such that the most common pixel variations are emphasized. The metrics were computed on 10 m Green and NIR bands of all Sentinel-2 scenes in SNAP using one pixel displacement over all angles in 5×5 pixel neighbourhoods and 32 bit quantization level with probabilistic quantizer.

2.6 Additional Predictors of Waterway Proximity

A set of waterway proximity layers were also derived for the classification in addition to the Sentinel-1 and Sentinel-2 features described above. It is clear that availability of aquatic breeding sites is a constraining factor for the distribution of the species, and inclusion of a waterway proximity layer in the predictor set thus allow the classifier to discriminate between suitable land covers with

and without potential breeding sites nearby. These waterway proximity layers were derived from OpenStreetMap (© OpenStreetMap contributors 2021) data. Raw OpenStreetMap data for Baden-Württemberg and neighbouring regions was downloaded in the PBF format from the download server of Geofabrik GmbH: https://download.geofabrik.de. Line features registered with the waterway tag as either: stream, brook (deprecated tag which was treated as equivalent to stream in this project, see: *OpenStreetMap Wiki* 2021), river, ditch, or drain, were first extracted. Extracted waterway features in culverts, tunnels, underground or pipelines were thereafter removed. The stream and brook tags are used for narrow natural waterways (*OpenStreetMap Wiki* 2021) and were assumed to represent the most common aquatic habitat used by the fire salamander (i.e. smaller fish-free streams Thiesmeier and Schuhmacher 1990). It was however unclear whether waterways registered as river or drainage ditches (ditch and drain tags) also offer potential breeding sites. Six different waterway layers, referred to as: *Stream*, *Stream-Ditch1*, *Stream-Ditch2*, *Stream-River*, *Stream-River-Ditch1*, and *Stream-River-Ditch2*, were therefore generated for further evaluation during the model selection process. An overview of the waterway tag combinations used in each layer is given in Table 2.3. The lines in each waterway layer were first buffered 50 m, and proximity maps of 10 m resolutions were thereafter generated with GDAL.

Table 2.3: Waterway tag combinations used in the waterway proximity layers derived for the classification.

Layer Name	OpenStreetMap Waterway Tags
Stream	stream, brook
Stream-Ditch1	stream, brook, ditch
Stream-Ditch2	stream, brook, ditch, drain
Stream-River	stream, brook, river
Stream-River-Ditch1	stream, brook, river, ditch,
Stream-River-Ditch2	stream, brook, river, ditch, drain

2.7 Image Segmentation for Superpixel-Based Classification

The application of superpixel-based image classification, in which the classification is performed on mean values of roughly equally sized regions of similar pixels rather than single pixels, was tested in the analysis. Note that object-based classification is a similar classification method, but, the term superpixel-based is here used to clarify that regions used in the classification do not represent meaningful features such as roads and houses visible in an image. Fire salamander home-range estimates

larger than the 10 m pixel resolution, and a superpixel-based approach thus offer the possibility to consider the characteristics in areas of more suitable sizes in the classification.

The partitioning of the study area into superpixels was performed with the Simple Linear Iterative Clustering (SLIC) segmentation algorithm which is a k-means clustering algorithm adapted to take both pixel values and spatial distance into account (Achanta et al. 2012). The segmentation is controlled by the number of k-means cluster centres initialized in a regular grid over the image, and a weight factor which defines the importance of spatial distance relative to distance in pixel values. The SLIC segmentation was performed on false colour composites of the 20 m (Band 11) SWIR, and the 10 m NIR and Red bands from the *2019 June 29* scene for the area covered by orbit 108, and of the *2018 April 27* scene for the part in orbit 65 not covered by orbit 108. A contrast stretch of each band was applied by linearly stretching pixel values between the 2nd and 98th percentiles to the range from 0 to 255 during the generation of the false colour composites, resulting in 8 bit colour images. The images were segmented with the SLIC implementation in the OpenCV library (Bradski 2000) using a region size of 10 pixels, ruler (i.e. the weight factor) of 100, and forced connectivity between superpixels with the default minimum element size of 25 %. A region size parameter of 10 results in roughly 1 ha large superpixels, and a ruler of 100 was selected based on visual evaluation of the segmentation result.

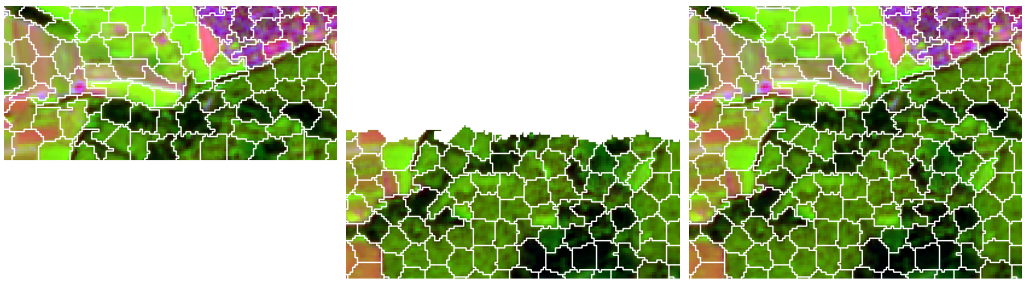

(a) Tile 1 segmentation. **(b)** Tile 2 segmentation. **(c)** Merged segmentation after sliver polygon removal.

Figure 2.8: Tile based SLIC segmentation on a subset of the *2019 June 29* false colour composite (R: SWIR, G: NIR, B: Red).

The segmentation of the *2019 June 29* scene had to be computed in two tiles due to the large image size. It was performed by extracting superpixels from the interior of the first tile processed and thereafter remove their area from the second tile (i.e. assign these pixels the no-data value) before its segmentation. This resulted in high agreement in the border regions between the two tiles, however, a few small (<10 pixels) sliver polygons were still present in the second segmentation (see

Figure 2.8b). These sliver polygons were merged with the neighbouring superpixel with the longest shared boundary, before the two segmentations were combined. Figure 2.8 provides a visualization of this tile based SLIC segmentation which also was used to combine the *2019 June 29* segmentation with the segmentation of the *2018 April 27* image. A final clipping of the full segmentation with the study area was further applied in order to force the superpixels to agree with the boundary of the study area, and small sliver polygons from this operation were also merged with neighbouring superpixels. Mean pixel values within the SLIC superpixels were thereafter derived and used as predictor variables for the superpixel-based classification approach.

2.8 Positive and Unlabelled Data

The positional accuracy of the fire salamander observations was insufficient for direct usage in the classification, and positive class samples, representing fire salamander habitats, were instead drawn from tree covered areas within 300 m of the observations. Forests are the most common terrestrial habitat of the fire salamander (Wagner et al. 2020) in Germany, and it is thus reasonable to assume that tree covered areas near the point observations represents suitable fire salamander habitats. A distance of 300 m was used since it was the largest coordinate uncertainty reported in the observation set. Identifying tree covered areas requires a tree cover mask, and it was derived from the *Tree Cover Density 2018* and *Forest Additional Support Layer 2018* products from the Copernicus Land Monitoring Service. A binary tree cover mask was first generated by applying a 30 % threshold on the tree cover density layer (in agreement with the threshold applied in the pan-European validation of the tree cover density product in CLMS 2021), and the forest additional support layer was then used to divide the tree cover mask into three layers of tree cover in urban, agricultural and forest context (urban context combined class 4 and 5 in the forest additional support layer). The geolocation accuracy in the satellite imagery and the tree cover masks can lead to tree covered pixels in the mask layers to be located outside the corresponding tree covered area in the imagery. This was prevented by reducing the size of each tree covered area in the mask layers with morphological erosion of one pixel size. The results were combined into a single tree cover mask, from which tree covered areas within a 300 m radius of fire salamander observations could be extracted.

A random selection of 10 % of the more than 2.8 million pixels located in tree covered areas within 300 m of the fire salamander observations were used as samples of the positive class in the pixel-based classification. This random selection was performed to generate a sample set that is representative of pixels within the tree covered areas but with a more manageable size. For the superpixel-based

classification, the positive class was sampled from the set of superpixels within 300 m of the observations which fulfilled tree cover overlap constraints of:

(i) 75 % or more of the superpixel area overlapped the tree covered area, or,

(ii) 75 % or more of a tree covered area overlapped the superpixel, and the tree covered area was larger than 25 % of the superpixel area.

50 % of the superpixels that fulfilled these constraints were randomly selected as the positive class for the superpixels-based classification, again to reduce the data set to a more suitable size.

The observations only contain information of locations where the fire salamander have been present, i.e. no absence observations were available. The classification is thus a one-class classification problem that can be approached with positive-unlabelled learning (PU-learning) methods. PU-learning use information from the positive class together with unlabelled samples, i.e. samples of unknown class label, which in SDM literature is called background or pseudo-absence data (Guisan et al. 2017). Unlabelled samples were generated by distributing points in a regular grid pattern with 1500 m × 1500 m point spacing throughout the study area. The 1500 m point spacing distance was selected in order to limit spatial auto-correlation between any point pair while still generating a large unlabelled set. Any grid point within 1500 m of a fire salamander observation was also removed from the unlabelled set. Unlabelled samples for the pixel-based classification was then extracted by selecting all pixels located within rectangular windows of 9×9 pixels centred at each grid point, while superpixels intersecting the grid points were selected as unlabelled samples for the superpixel-based classification.

2.9 Train and Test Areas

For evaluation of different modelling methods, it is important to split the data into a train set used for model fitting and a test set used for model evaluation. These sets should be independent of each other such that the test set represent unseen data, however, spatial auto-correlation makes it difficult to generate fully independent sets in practice. For this analysis, a set of subregions within the study area was used as test area for model evaluation. These test areas were generated by first distributing points in a diagonal grid with point spacing of 50 000 m × 50 000 m over the study area. The grid points were then buffered twice using radii 5000 m, and 6500 m, where the smaller radius defines the test area and the larger radius forms a buffer zone between the test and train areas used to reduce spatial auto-correlation between the sets. 16 test areas were generated in this fashion and their distribution can be seen in Figure 2.9.

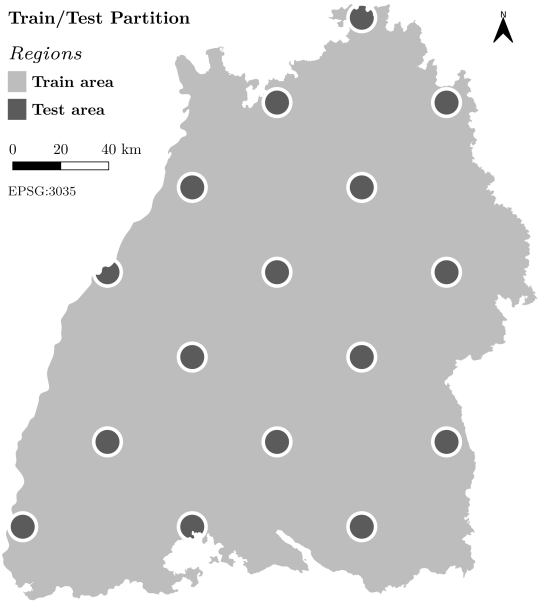

Figure 2.9: Train and test areas. Positive and unlabelled samples extracted from the train area were used for model fitting and selection, whereas the test area was used for model evaluation.

Train samples for both classification methods were selected as samples from the sets of positive and unlabelled data completely within the train area, while a unique test set for evaluation was created within the set of test areas. Positives in the test set were generated by distributing 1000 random points in the area of intersection between the tree covered areas within 300 m of fire salamander observations and the superpixels which fulfilled the overlap conditions used in the superpixel selection. Unlabelled test samples were generated by random sampling of 10 000 points in test areas more than 300 m away from any fire salamander observation point. From the unlabelled points in the test set, a subset of all points within areas of the tree cover mask was further selected (referred to as the tree cover test subset) for evaluation over tree covered areas only.

2.10 Model Fitting

Several classifiers can be used in PU-learning problems and balanced random forest (Chen et al. 2004) was selected for this project. Random forest is popular for remote sensing image classifications, partly since the method provide good classification results, but also since it can handle large data sets efficiently and has low sensitivity to the high dimensionality often present in remote sensing data

sets (Belgiu and Drăguţ 2016). It is based on decision tree bagging, in which the prediction is a combination of the predictions from a collection of decision trees trained on bootstrap samples (observations sampled with replacement), but only search tree splits over random predictor subsets in order to reduce correlation between trees (Breiman 2001). Balanced random forest counter class imbalances in the data by creating balanced bootstrap samples, and relates with bagging based approaches in PU-learning literature. Mordelet and Vert (2014) motivated bagging in PU-learning problems since bootstrap samples of the unlabelled set contain different amount of true positives and thus decrease correlation between classifiers. They further showed that bagging of one-class support vector machines, trained on the full positive set and bootstrap samples of given size from the unlabelled data, gave competitive results compared to other PU-learning methods. If a similar bagging based approach is applied but with decision tree classifiers, in which each tree split is searched for over a random predictor subset, and with bootstrap samples drawn from both the positive and the unlabelled sets, then the method is a balanced random forest.

Model fitting and selection was performed in scikit-learn using the balanced random forest implementation in imbalanced-learn (Lemaître et al. 2017). The models were trained on bootstrap samples of the positive class and equally sized bootstrap samples of the unlabelled class for each decision tree. The random predictor subset size used for tree splits was set to the square root of the number of predictor variables (rounded downwards to the nearest integer), in agreement with the recommended default settings for classifications (Hastie et al. 2009). Variable reduction was not applied, but, combinations of different predictor sets were evaluated using 5-fold cross-validation on models trained with a 100 trees. 5-fold cross-validation is a method to estimate how well a model perform on new data using only the train set, and it can therefore indicate whether a model tend to overfit the train data. This was performed in two steps, first, the combination of Sentinel-1 images, Sentinel-2 bands, texture and vegetation indices were considered as predictors, and it was from this test found that the best models were the full model which included all predictors. However, it should be noted that models based solely on Sentinel-2 bands performed almost as well. All predictors were kept for the second step in which the addition of different waterway proximity layers were evaluated. Inclusion of waterway proximity layers improved model prediction, and the largest improvement was found with the *Stream* and *Stream-River* layers. The *Stream-River* layer was finally selected for the final models since it appeared to be most beneficial for models in the orbit overlap area. The complete result of the 5-fold cross-validation is available in Appendix A.

Final models were thereafter generated using balanced random forests with 300 trees. Due to the coverages of the Sentinel-2 orbits, three models were fitted for

both the pixel-based and the superpixel-based approach: one for orbit 65, one for orbit 108, and one for the orbit overlap area as shown in Figure 2.6. The model in the overlap area benefit from having all predictor variables available, whereas single orbit models includes data from larger areas. Fusion of the three model predictions was performed by averaging the predicted class probabilities. This made it possible to generate final prediction maps of fire salamander habitat suitability covering the full study area.

2.11 Model Evaluation and Exploration

Evaluation of the final prediction maps were performed with the Receiver Operating Characteristics (ROC) curve and the area under curve (AUC) metric (see: Fawcett 2006 for an overview of ROC analysis). Both the full test set and the tree cover test subset, which only include samples located within the tree cover mask, were used in the evaluation. A ROC curve contrast true positive rate: proportion of test set positives classified as positives, against false positive rate: proportion of test set unlabelled samples classified as positives, over varying threshold values used to map predicted class probabilities into binary predictions. The AUC metric is thereafter calculated as the area under the plotted ROC curve and is a commonly used metric in SDM evaluations (Elith et al. 2006). It can be interpreted as the probability that a randomly selected positive sample in the test set is predicted to have higher positive class probability than a randomly selected unlabelled sample in the test set (Fawcett 2006), and take a maximum value of 1 for a perfect classifier, and a value of 0.5 for a random prediction.

A land cover based model at 100 m pixel resolution was also created for comparison using the *Stream-River* proximity layer combined with data from Copernicus Land Monitoring Service. This model, hereafter referred to as the LC-based classification, provides a baseline in the evaluation for how well the information available in the land cover data sets can explain the distribution of positive samples. The LC-based model was derived with the same balanced random forest classifier as used in the image classifications trained on 1000 random points sampled within the tree cover areas of positive class, and the set of gridded unlabelled points. Land cover data included in the model consisted of the *Broadleaf Cover Density 2018*, *Coniferous Cover Density 2018*, *Imperviousness Degree 2018* layers, as well as *Grassland 2018* and classes of "Arable land" and "Permanent crops" from *CORINE Land Cover 2018* aggregated from 10 m to 100 m resolution with average resampling.

An exploratory analysis of the image classifications was finally applied to offer better understanding of the model predictions in different forest types, and how distance to the *Stream-River* layer influence the prediction. The influence of the

Stream-River layer was first evaluated with partial dependence plots using the model train data. The forest type exploration was thereafter based on a point set of land cover observations within the study area from the Land Use and Coverage Area frame Survey (LUCAS) of Eurostat (2018a). The LUCAS survey points contain detailed land cover information for each point location derived from *in situ* and photo-interpreted observations. Points with *Stream-River* proximity of 200 m or less were used in the exploration since the *Stream-River* layer partial dependence plots were relatively stable for these distances, which thus reduce variation in predicted probabilities caused by the *Stream-River* proximity layer. Classes of broadleaved, coniferous, and mixed woodlands, for which woodland is defined as tree covered areas with a canopy cover of more than 10 % (Eurostat 2018b), were considered in the analysis which was performed by computing histograms of the predicted habitat suitability for each class. The primary land cover at the theoretical point location was used and only points in which the primary land cover represented more than 90 % of the land cover at the location were included.

3 Results

3.1 Model Evaluation and Comparison

The ROC curves generated for model evaluation is presented in Figure 3.1. These graphs show that the models are able to discriminate well between positive and unlabelled samples in the full test set with AUC values around 0.9, representing the overall model performance in test areas. Superpixel-based classification appear to perform slightly better than the pixel-based approach, which further performs better than the LC-based model. The graphs further include the ROC curve of the *Stream-River* proximity layer only, and it is noticeable that it explains the positive sample distribution relatively well, but, additional land cover information still improves the predictions. It is however expected that all models perform well in non tree covered unlabelled samples, resulting in high AUC values over the full test set. The tree cover test subset was therefore used to evaluate the predictions in tree covered areas only, since discrimination between positive and unlabelled samples in these areas is expected to be more difficult. It is clear from the ROC curves over the tree cover test subset that the pixel-based method performs slightly better than the LC-based model, while the superpixel-based classification outperform both of them.

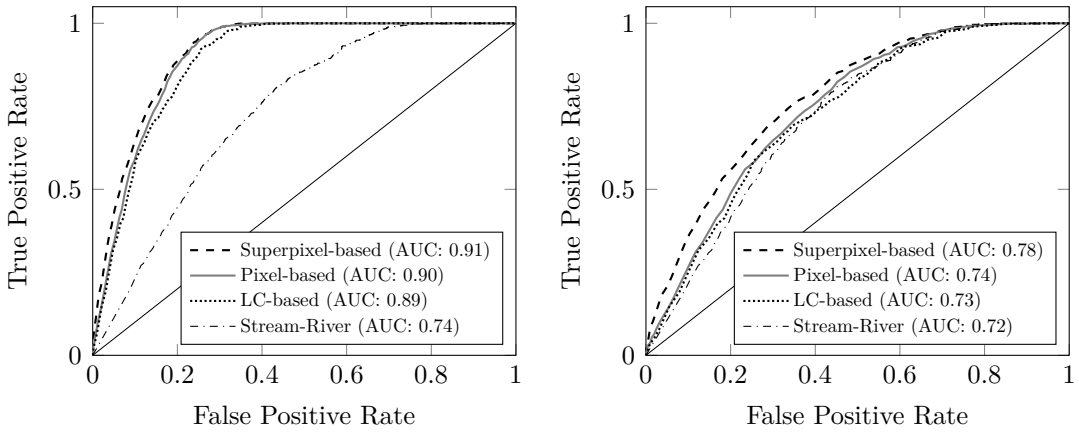

(a) Full test set.

(b) Tree cover test subset.

Figure 3.1: ROC curves and AUC scores for the pixel and superpixel-based classifications contrasted against the LC-based model which is built with land cover data. The Stream-River curve shows the performance of the *Stream-River* proximity layer only. The full test set (a) compare samples from tree covered areas within 300 m of fire salamander observations against unlabelled samples throughout the study area, while the tree cover test subset (b) contains only unlabelled samples within tree covered areas.

3.2 Resultant Prediction Maps

Maps of predicted positive class probability, here interpreted as habitat suitability for the fire salamander, from the two image classification models are presented in Figures 3.2 and 3.3. The prediction maps have been overlaid with the fire salamander observation set from Figure 2.2, which for visualisation purposes have been buffered 1 km. The distribution of predicted habitat suitability from both classifications appear to agree well with the fire salamander observation set, and a high agreement between both predictions can be noticed in general.

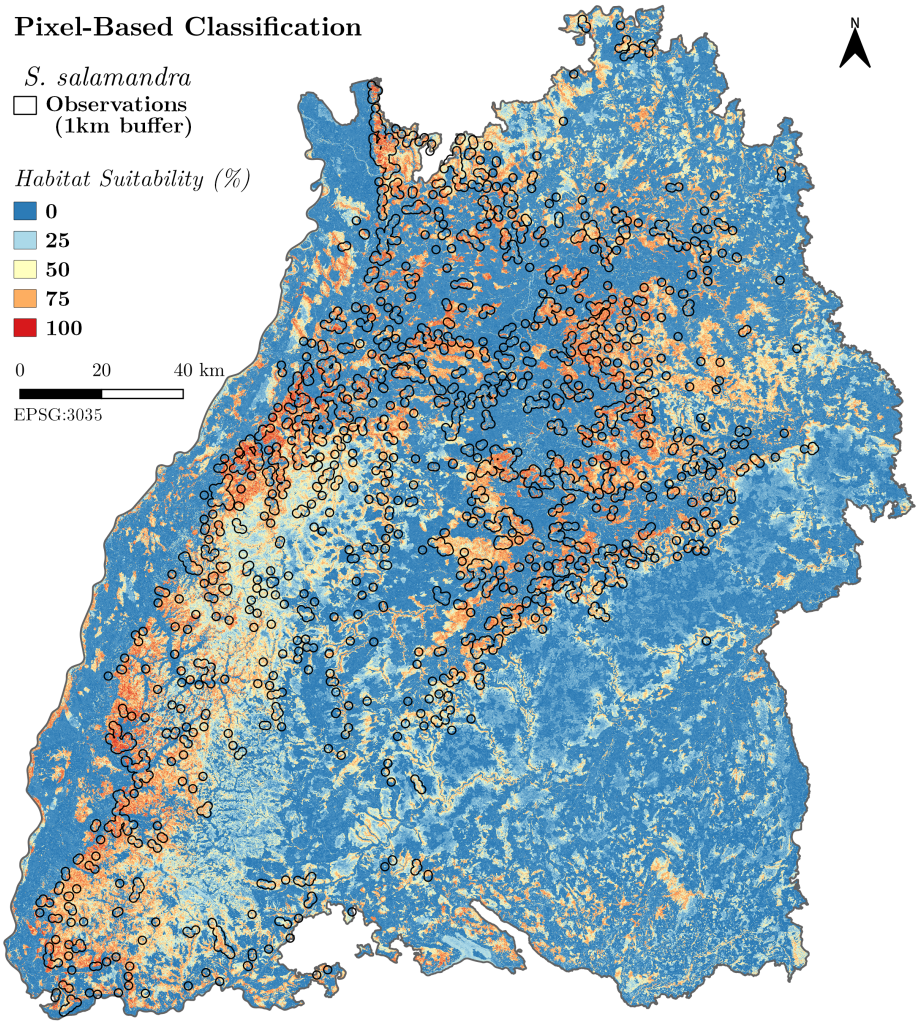

Figure 3.2: Resultant habitat suitability map from the pixel-based classification. The map displays predicted positive class probability (%) from the balanced random forest classifier, which is interpreted as fire salamander habitat suitability. Transparent regions with dark boundaries represent 1 km buffer zones of the fire salamander observation set used in the classification.

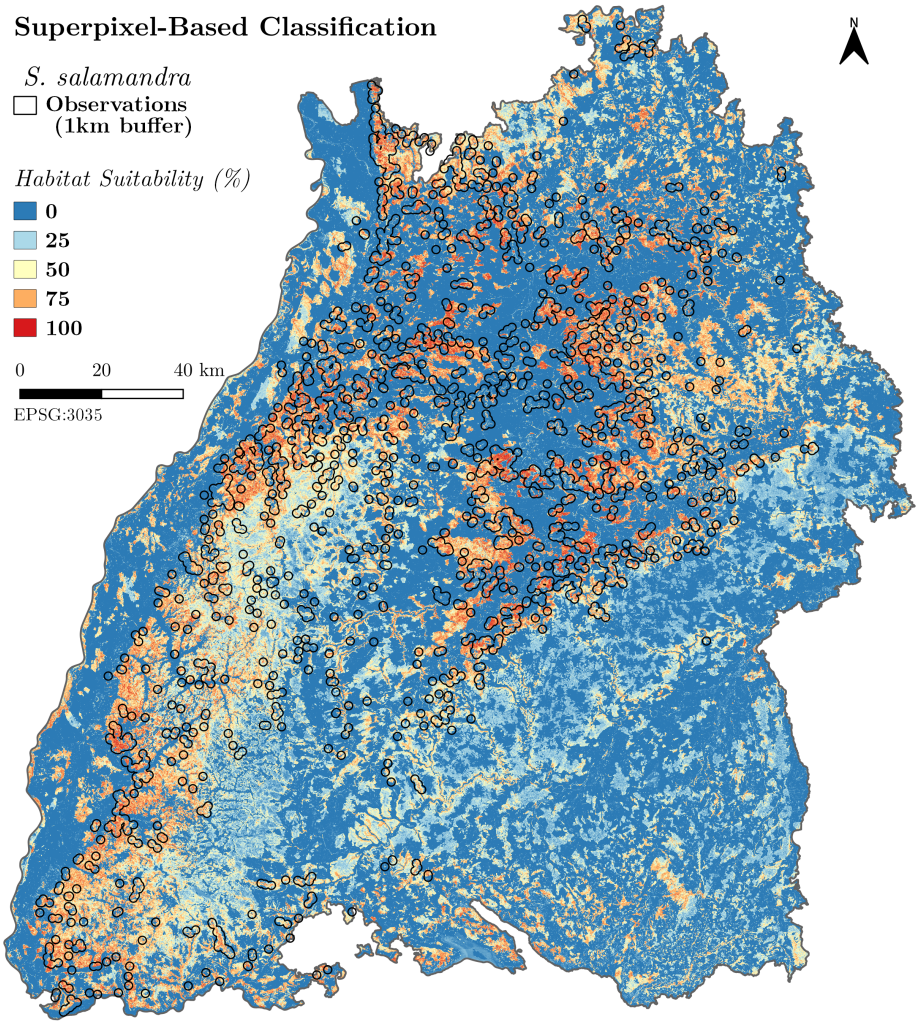

Figure 3.3: Resultant habitat suitability map from the superpixel-based classification. The map displays predicted positive class probability (%) from the balanced random forest classifier, which is interpreted as fire salamander habitat suitability. Transparent regions with dark boundaries represent 1 km buffer zones of the fire salamander observation set used in the classification.

3.3 Model Exploration

Partial dependence plots of the *Stream-River* layer is presented in Figure 3.4. The graphs show how the prediction depends on the *Stream-River* proximity layer over all three models fitted in the different orbit areas for both the pixel-based and the superpixel-based approach. Note that lines in the *Stream-River* layer was buffered 50 m before the proximity layer was generated, and that distances are measured from this buffer zone. The graphs indicate a decrease in predicted habitat suitability with increasing distances in the *Steam-River* proximity layer. The decrease appear to start at about 200 m *Stream-River* proximity and then flatten out near 500 m. A negative correlation between distance to streams and rivers which can be used as breeding sites for the fire salamander is expected, and the results indicate that the area within roughly 200 m from these features were predicted with the highest habitat suitability. However, positives for the classifications were sampled from tree covered areas within 300 m of fire salamander observations, and if a large part of the observations are of larvae in streams, then this sampling will result in high suitability values at *Stream-River* proximity values shorter than 300 m. Note that it was for most observations not known whether an adult or a larva had been observed. The partial dependence plots thus show a pattern that can be expected due to the sampling of positives, which must be considered during evaluation of the plots.

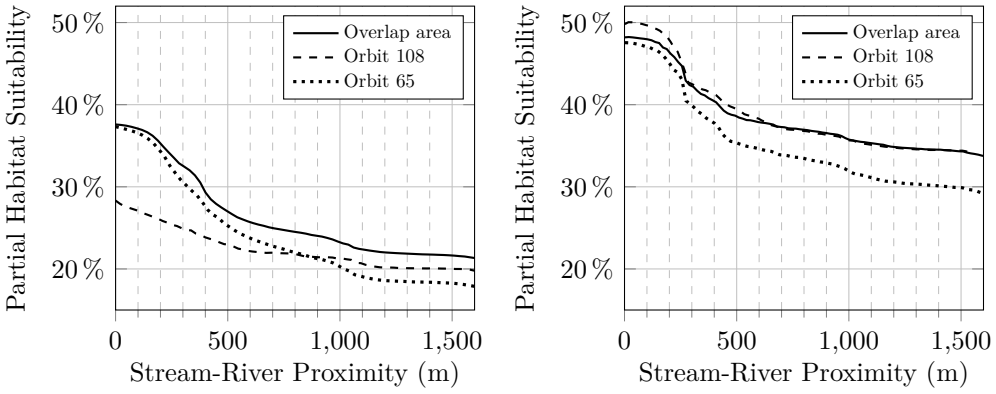

(a) Pixel-based.

(b) Superpixel-based.

Figure 3.4: *Stream-River* layer partial dependence plots from pixel-based (a) and superpixel-based (b) classifications over each orbit area. These plots indicates how the predictions depend on the *Stream-River* proximity layer. The *Steam-River* proximity layer contain distances to a 50 m buffer around OpenStreetMap waterways registered with stream, brook, and river waterway tags.

Histograms showing the count of predicted habitat suitability values in LUCAS 2018 survey points of different woodland classes with *Stream-River* proximity

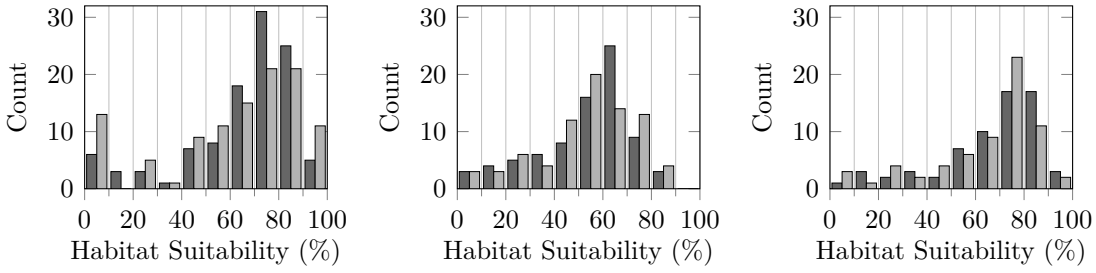

(a) Broadleaved woodland. **(b)** Coniferous woodland. **(c)** Mixed woodland.

Figure 3.5: Histograms of predicted habitat suitability in LUCAS *in situ* or photo-interpreted points with *Stream-River* proximity of ≤200 m and with more than 90 % of the primary land cover classified as broadleaved (a), coniferous (b), or mixed (c) woodland classes. Histograms from the pixel-based classification is presented in dark grey, while histograms from the superpixel-based classification is presented in light grey.

of 200 m or less is presented in Figure 3.5. Comparison in these points reduce prediction differences caused by the *Stream-River* layer since the partial dependence plots in Figure 3.4 are relatively stable at distances below 200 m. However, land cover dependent differences can still be present. The woodland class in the LUCAS survey is defined as tree covered areas with a canopy coverage of minimum 10 %, and the broadleaved and coniferous woodland classes are used for areas where 75 % or more of the canopy is composed by either tree type (Eurostat 2018b). The mixed woodland class is further used for areas with more than 25 % of the canopy from each tree type. Note that this woodland class definition do not distinguish between forest and other tree covered areas, and thus only indicates tree cover within an area. It can be seen that points from broadleaved areas are predicted with higher habitat suitability values than points from coniferous areas. Tree covered areas of mixed class are also classified with suitability values similar to broadleaved areas, which thus suggests that these areas contain sufficient amount of broadleaved trees (>25 % of the canopy) to be predicted as suitable habitats.

4 Discussion

4.1 Model Comparison

The ROC analysis (Figure 3.1) showed that pixel-based and superpixel-based remote sensing image classification methods performed better than the model based on only land cover classification data. The evaluation was based on how well the models were able to discriminate between tree covered areas within 300 m of fire salamander observations (positive class representing fire salamander habitats), and unlabelled samples from other areas further away than 300 m from the observations. The test set used for the evaluation is thus expected to contain fire salamander habitats in the unlabelled samples, but, it is further possible that the positive class set is contaminated with areas that are unsuitable to the fire salamander. It is preferable to have a test set without these contaminations, however, since the models were trained to discriminate between positive and unlabelled samples with the same type of contaminations, it is also applicable to evaluate the models after their ability to do so. The model based on land cover classification data provides a baseline model used to compare the image classifications with a model of similar information, i.e. waterway proximity and land cover information. It should not be interpreted as a typical correlative SDM, which traditionally has been built with predictors describing climatic conditions either directly or indirectly through topographic variables (Franklin 2010). The results nevertheless indicate that high resolution remote sensing imagery can be used to build fire salamander habitat suitability models with better discriminatory performance compared to models built with common land cover classification products.

The reason why the image classification approaches performed better than the land cover classification based model is likely explained by the detailed information available in high resolution remote sensing imagery. A model based on available land cover classification layers is highly dependent on the information classes used during the classification. These are not necessarily designed to represent the habitat type of interest in the modelling, and they can further contain erroneous classifications which affect the model prediction. This is especially clear in forest areas where

minor difference in the amount of broadleaved and coniferous trees can result in different classifications due to threshold based information class definitions. Remote sensing images do not contain classification errors and their accuracy instead depend on the accuracy of the measurement with corrections applied, as well as the geolocation accuracy. Co-registration can however reduce the influence of geolocation accuracy, and it can be performed with relatively automatic methods as in this project. Cloud cover in optical imagery is nevertheless a problematic issue for classifications over large study areas. Images from single acquisition dates were used in this project since multiple scenes with no or low amount of cloud cover could be identified, however, this further required data fusion over the Sentinel-2 orbits, which was applied by decision level fusion. An alternative is to use time-series image composites (e.g. see: Griffiths et al. 2019) rather than images from single acquisition dates, which remove influence of cloud cover and makes it possible to train classifiers over the full study area. Phenological differences at tree species level may not be possible to distinguish in time-series composites, but, it is not clear whether this was necessary for the classification.

The evaluation further showed that the superpixel-based approach performed better than the pixel-based classification. Superpixel-based classification was motivated because the average fire salamander home ranges are larger than the pixel size of 10 m resolution (Burgstaller et al. 2021; Hendrix et al. 2017; Schulte et al. 2007). SLIC segmentation oversegment homogeneous areas and create approximately equally sized regions of similar pixels. This is in contrast to traditional object-based methods in which the segmentation is used to derive meaningful features (objects representing e.g. a road, a house, etc.) from the image such that object size and shape can be taken into account during the classification (Blaschke et al. 2014). However, object size and shape was not suitable to consider in this project since the true habitat area each fire salamander observation represent was unknown, and a SLIC superpixel-based method was thus more appropriate for this study. SLIC superpixel-based land cover classification has in addition been found to achieve similar results as an object-based classification (Csillik 2017). An important benefit of SLIC superpixel-based compared to pixel-based classification is that the segmentation results in a smaller data set size and thus also a simpler model fitting process. The resultant prediction map also contains less salt-and-pepper noise, which may be the main reason why the superpixel-based classification performed better than the pixel-based approach in this project. It is also possible that the larger subset size (50 %) of positive samples used in the superpixel-based approach better captured the positive class distribution than the selected subset of positive pixels (10 %) used in the pixel-based classification. This was however possible due to the reduced data set size obtained after the SLIC segmentation. Superpixel-based classification thus offer benefits which can lead to

improved classifications, and it is therefore recommended to further evaluate its usage in habitat suitability studies.

4.2 Distribution of Fire Salamander Habitat Suitability

The final prediction maps in Figure 3.2 and Figure 3.3 presents distributions of land cover with suitable habitats for the fire salamander throughout Baden-Württemberg, and these distributions appear to agree well with the distribution of fire salamander observations used in this study. It is nevertheless possible to identify areas predicted with high habitat suitability but without any fire salamander observation in the nearby region, such as Kaiserstuhl and other tree covered regions in the Upper Rhine Plain. This can occur under three different scenarios:

(i) the fire salamander is present, but an observation has not been recorded,

(ii) the fire salamander is absent, but the area is suitable for the species, or

(iii) the fire salamander is absent, and the area is not suitable for the species.

Scenario ii may for example occur if migration barriers have restricted the fire salamander from the area, while scenario iii is more related to limitations in the modelling. These models were designed to predict how suitable the land cover in an area is for the fire salamander, but also took into consideration the distance to stream and river features (i.e. potential breeding sites). Since other factors that may constrain the fire salamander distribution e.g. soil type, hydrological conditions, pollution, etc. are not accounted for in the models, the final prediction maps are expected to overestimate the true distribution of suitable habitats for the fire salamander in Baden-Württemberg.

The models can further falsely predict an area as unsuitable for the fire salamander. Inclusion of the *Stream-River* proximity layer in the models is expected to lead to an overprediction of habitat suitability in general, since not all stream or river sections are expected to offer potential breeding sites to the fire salamander. On the other hand, areas without stream and river features but with aquatic breeding sites of other types, e.g. forest road ditches, can be misclassified as unsuitable for the fire salamander. Note that this can also be caused by erroneous registrations in the OpenStreetMap data. The 5-fold cross-validation however indicated that inclusion of the *Stream-River* layer in the models improved the predictions, which motivates its inclusion even though it may come at the expense of misclassifying a few areas as unsuitable.

4.3 Suitable Habitats for the Fire Salamander in Baden-Württemberg

An image classification approach to model habitat suitability provides less explanation compared to models built with ecologically meaningful predictors, but, some model exploration could still be performed. The main issue is to reduce the influence of additional predictors while exploring the prediction in different land cover types. For this analysis, the additional predictor set consisted only of the *Stream-River* proximity layer, and its influence on the prediction was limited by evaluating the prediction in LUCAS points within a relatively homogeneous range of the *Stream-River* layer partial dependence plot. However, other methods must be considered for larger sets of additional predictors.

The curves in the *Stream-River* partial dependence plots in Figure 3.4 suggested a decrease in predicted habitat suitability beginning at around 200 m *Stream-River* proximity which thereafter flattens out near 500 m. Ficetola et al. (2012) analysed the results of six capture-recapture studies and found that 96 % of the fire salamanders studied moved less than 200 m, 2 % moved distances between 200 m to 500 m and 2 % moved longer distances than 500 m. Similar results were also found in the more recent study by Kiss et al. (2021), while Hendrix et al. (2017) reported slightly larger proportions of longer movements, with the longest distance moved reaching 1.9 km. Although the partial dependence plots agree well with these studies, it is likely that the partial dependence curves simply reflect the method used to sample positives for the classification. This is because observations of larvae in streams will result in a preference for *Stream-River* proximity values below 300 m, which corresponds well with the curves in the partial dependence plots. It should further be considered that the *Stream-River* proximity layer only contain rough estimates of distances to the area around the nearest stream and river feature registered in OpenStreetMap rather than known suitable aquatic habitats for the fire salamander, and that distances are measured along a straight line without taking any migration barriers along the path into account. The results thus show that the models predicted high habitat suitability in areas within roughly 200 m of stream and river features, but, it is not clear whether this reflects fire salamanders habitat preferences or rather the method used to sample positives for the classification.

The histograms of predicted habitat suitability in different LUCAS 2018 survey woodland points presented in Figure 3.5 indicate how the models predicted habitat suitability in tree covered areas of different tree types. Woodland areas in the LUCAS survey are defined as tree covered areas with more than or equal to 10 % canopy cover. This definition does not agree with the definition of "other wooded land" by the Food and Agriculture Organization of the United Nations (FAO), and

the LUCAS woodland points are therefore more appropriate to consider as points in tree covered areas. LUCAS points in which the canopy is composed of 75 % or more broadleaved trees were classified with higher suitability values than points with 75 % or more coniferous trees. This is in line with larger fire salamander populations in broadleaved compared to coniferous forests as indicated by the larval abundance analysis in Wagner et al. (2020). It emphasizes the importance of forest management practices for conservation of the species, and especially conversion from broadleaved to coniferous forest lead to decreased habitat suitability, which may result in population declines as discussed in Schmidt et al. (2005). Mixed forests appear suitable to the fire salamander on the other hand, since LUCAS points with mixed tree types (canopy composed of 25 % or more of both coniferous and broadleaved trees) were classified with high suitability values similar to areas with broadleaved tree cover.

The model prediction relates with the more common land cover characteristics found within the set of positive samples in the classification. Image classification with high resolution imagery require high positional accuracy in the observation set, which the fire salamander observations could not fulfil. This issue was handled by sampling positives from tree covered areas near the observations which required previous knowledge regarding the habitat preferences of the fire salamander habitat as well as a large observation set. Sampling positives from tree covered areas near fire salamander observations most likely include unsuitable areas in the positive set, but, the more common land cover characteristics within this set of positives are more important to the classifier and should thus obtain higher suitability values. Assuming that the most common land cover types found in the positive set indeed represent the most suitable habitat for the fire salamander, then, the model exploration indicates that tree covered areas with a canopy composed of more than 25 % of broadleaved trees are the most suitable terrestrial environment for the fire salamander in Baden-Württemberg.

4.4 Image Classification for Habitat Suitability Modelling

Habitat suitability models built with already available land cover classification products require limited data processing and allows easy interpretations of relationships between species observations and land cover variables. However, these models depends on the information classes used during the land cover classification which may not correspond with the habitat of interest as previously mentioned. Remote sensing based habitat suitability models counter this issue by including an intermediate processing step in which more representative land cover products are

derived (He et al. 2015). In contrast, the image classification methods applied in this project remove this intermediate processing step and thus avoid introducing any classification errors in the predictor variables. The drawback is that this results in limited model interpretation since the predictors are not ecologically meaningful.

Image classification should be considered as a method to identify suitable habitats in land covers directly from remote sensing imagery, whereas SDM is a more general approach applied to model the potential distribution of a species based on environmental predictors. Focusing only on habitat suitability in land covers is thus a simpler problem, but, the models can still provide important information for species conservation. For the fire salamander, the high evaluation score obtained in all models indicated that land cover and waterway proximity explained the distribution of fire salamander observations in Baden-Württemberg well, thus, motivating image classification as a method to model fire salamander habitat suitability. Image classification is further applicable for similar projects at regional or local scales in which land covers suitability for the species is of interest and when remote sensing imagery can provide more information than land cover classification products.

4.5 Additional Considerations

The balanced random forest classifier was suitable for the classification due to its ability to handle the high dimensionality and multi-collinearity in the data set. No variable reduction was applied, but, the 5-fold cross-validation used in the model selection process (see: Appendix A) indicated that inclusion of texture and vegetation indices slightly improved the models, although, models based only on Sentinel-2 bands resulted in high cross-validation scores as well. Inclusion of texture and vegetation indices increase the dimensionality and multi-collinearity of the predictor set, and the result of the cross-validation indeed show that random forest is relatively insensitive to these issues and avoids overfitting the data, in agreement with previous studies (Belgiu and Drăguţ 2016). However, feature reduction is still suitable since it may improve classifications (Belgiu and Drăguţ 2016), and also reduces the data set size. This was not performed in the analysis but is recommended for similar studies.

The 5-fold cross-validation further showed that Sentinel-2 data was most important for the classification. This was expected since Sentinel-2 images contain more information than Sentinel-1 scenes. Inclusion of Sentinel-1 scenes in this type of classification is nevertheless motivated by the backscattered signal's dependence on the vegetation density (Dostálová et al. 2021). However, the applied IDAN speckle filter reduced the spatial resolution in the images in order to counter speckle noise and thus also reduced the possibility to identify smaller backscatter differences

within forest areas. It is therefore likely that metrics from Sentinel-1 time-series data as presented in Dubois et al. (2020) would have provided more useful information to the classifier compared to the multi-temporal image set used, since it allows speckle filtering to be applied in temporal rather than spatial dimension. This requires additional data processing but may lead to an improved classification.

5 Conclusions

Land covers in Baden-Württemberg were classified after their habitat suitability for the fire salamander using pixel-based and superpixel-based image classification methods. The classifications obtained higher evaluation scores than a model based on available land cover classification products, which therefore motivate the use of image classification in habitat suitability studies. The methods are applicable for projects at regional to local mapping scales in which the focus is to predict how suitable different land covers types are for a species. The superpixel-based model obtained a slightly higher AUC score than the pixel-based model, it is thus recommended to further evaluate superpixel-based habitat suitability classification in future studies. Model exploration based on LUCAS 2018 survey points further indicated that the models predicted high suitability in tree covered areas located roughly 200 m or less from stream and river features, with a canopy cover of at least 10 %, and with more than 25 % of broadleaved trees in the canopy composition.

References

© European Union, Copernicus Land Monitoring Service (2018). European Environment Agency (EEA). URL: https://land.copernicus.eu/ (visited on 10/15/2021).

© OpenStreetMap contributors (2021). *Data retrieved from https://download.geofabrik.de*. (Visited on 10/15/2021).

Achanta, R. et al. (2012). "SLIC Superpixels Compared to State-of-the-Art Superpixel Methods". In: *IEEE Transactions on Pattern Analysis and Machine Intelligence* 34.11, pp. 2274–2282. DOI: 10.1109/TPAMI.2012.120.

Antzen, J. W. and J. van Belkom (2020). "'Mainland-island' population structure of a terrestrial salamander in a forest-bocage landscape with little evidence for *in situ* ecological speciation". In: *Scientific Reports* 10, 1700. DOI: 10.1038/s41598-020-58551-0.

Bani, L. et al. (2015). "Ecological connectivity assessment in a strongly structured fire salamander (*Salamandra salamandra*) population". In: *Ecology and Evolution* 5.16, pp. 3472–3485. DOI: 10.1002/ece3.1617.

Belgiu, M. and L. Drăguţ (2016). "Random forest in remote sensing: A review of applications and future directions". In: *ISPRS Journal of Photogrammetry and Remote Sensing* 114, pp. 24–31. DOI: 10.1016/j.isprsjprs.2016.01.011.

Beukema, W., J. Erens, et al. (2021). "Landscape epidemiology of Batrachochytrium salamandrivorans: reconciling data limitations and conservation urgency". In: *Ecological Applications* 31.5, e02342. DOI: 10.1002/eap.2342.

Beukema, W., A. Martel, et al. (2018). "Environmental context and differences between native and invasive observed niches of *Batrachochytrium salamandrivorans* affect invasion risk assessments in the Western Palaearctic". In: *Diversity and Distributions* 24.12, pp. 1788–1801. DOI: 10.1111/ddi.12795.

Blaschke, T. et al. (2014). "Geographic Object-Based Image Analysis – Towards a new paradigm". In: *ISPRS Journal of Photogrammetry and Remote Sensing* 87, pp. 180–191. DOI: 10.1016/j.isprsjprs.2013.09.014.

Blaustein, A. R. and J. M. Kiesecker (2002). "Complexity in conservation: lessons from the global decline of amphibian populations". In: *Ecology Letters* 5.4, pp. 597–608. DOI: 10.1046/j.1461-0248.2002.00352.x.

Bradski, G. (2000). "The OpenCV Library". In: *Dr. Dobb's Journal: Software Tools for the Professional Programmer* 25.11.

Breiman, L. (2001). "Random Forests". In: *Machine Learning* 45, pp. 5–32. DOI: 10.1023/A:1010933404324.

Burgon, J. D. et al. (2021). "Phylogenomic inference of species and subspecies diversity in the Palearctic salamander genus *Salamandra*". In: *Molecular Phylogenetics and Evolution* 157, 107063. DOI: 10.1016/j.ympev.2020.107063.

Burgstaller, S. et al. (2021). "Demography and spatial activity of fire salamanders, *Salamandra salamandra* (Linnaeus, 1758), in two contrasting habitats in the Vienna Woods". In: *Herpetozoa* 34, pp. 23–34. DOI: 10.3897/herpetozoa.34.e58496.

Catenazzi, A. (2016). "Ecological implications of metabolic compensation at low temperatures in salamanders". In: *PeerJ*, 4:e2072. DOI: 10.7717/peerj.2072.

Chen, C., A. Liaw, and L. Breiman (2004). *Using Random Forest to Learn Imbalanced Data*. Technical Report. Berkeley, Department of Statistics, University of California.

Collecte Localisation Satellites (CLS) (2016). *Sentinel-1 Product Definition*. Product Document Ref. S1-RS-MDA-52-7440. European Space Agency ESA. Issue: 2.7.

Copernicus Land Monitoring Service (CLMS) (2021). *HRL Forest 2018 Product User Manual. Tree-cover/forest and change 2015-2018*. Version 1.2. European Environment Agency (EEA). 68 pp. URL: https://land.copernicus.eu/user-corner/technical-library.

Copernicus Sentinel 2 Mission Performance Centre (S2 MPC) (2020). *Sen2Cor Software Release Note*. Technical Document Ref. S2-PDGS-MPC-L2A-SRN-V2.9.0. European Space Agency ESA. Issue: 01.

Copernicus Sentinel 2 Mission Performance Centre (S2 MPC) (2021). *Level 2A Data Quality Report*. Technical Document Ref. S2-PDGS-MPC-L2ADQR. European Space Agency ESA. Issue: 41.

Csillik, O. (2017). "Fast Segmentation and Classification of Very High Resolution Remote Sensing Data Using SLIC Superpixels". In: *Remote Sensing* 9.3, 243. DOI: 10.3390/rs9030243.

Dostálová, A. et al. (2021). "European Wide Forest Classification Based on Sentinel-1 Data". In: *Remote Sensing* 13.3, 337. DOI: 10.3390/rs13030337.

Dubois, C. et al. (2020). "CHARACTERIZATION OF LAND COVER SEASONALITY IN SENTINEL-1 TIME SERIES DATA". In: *ISPRS Annals of the Photogrammetry, Remote Sensing and Spatial Information Sciences* V-3-2020, pp. 97–104. DOI: 10.5194/isprs-annals-V-3-2020-97-2020.

Dufresnes, C. (2019). *Amphibians of Europe, North Africa and the Middle East : A Photographic Guide*. London: Bloomsbury Wildlife. ISBN: 978-1-4729-4139-8.

Elith, J. et al. (2006). "Novel methods improve prediction of species' distributions from occurrence data". In: *Ecography* 29.2, pp. 129–151. DOI: 10.1111/j.2006.0906-7590.04596.x.

Escoriza, D. and A. Hernandez (2021). "Buffered microclimate determines the presence of *Salamandra corsica*". In: *Journal of Forestry Research* 32, pp. 1089–1093. DOI: 10.1007/s11676-020-01142-6.

European Space Agency (ESA) (2021). *Sentinel Online. Sentinel-1 SAR User Guide*. URL: https://sentinel.esa.int/web/sentinel/user-guides/sentinel-1-sar (visited on 11/19/2021).

Eurostat (2018a). *LUCAS micro data 2018*. URL: https://ec.europa.eu/eurostat/web/lucas/data/primary-data/2018.

Eurostat E4.LUCAS (ESTAT) (2018b). *LUCAS 2019 (Land Use / Cover Area Frame Survey). Technical reference document C3: Classification (Land cover & Land use)*. Technical Report.

Fawcett, T. (2006). "An introduction to ROC analysis". In: *Pattern Recognition Letters* 27.8, pp. 861–874. DOI: 10.1016/j.patrec.2005.10.010.

Ficetola, G. F. et al. (2012). "Can patterns of spatial autocorrelation reveal population processes? An analysis with the fire salamander". In: *Ecography* 35.8, pp. 693–703. DOI: 10.1111/j.1600-0587.2011.06483.x.

Fischler, M. A. and R. C. Bolles (1981). "Random Sample Consensus: A Paradigm for Model Fitting with Applications to Image Analysis and Automated Cartography". In: *Communications of the ACM* 24.6, pp. 381–395. DOI: 10.1145/358669.358692.

Food and Agriculture Organization of the United Nations (FAO) (2018). *Global Forest Resources Assessment 2020. Terms and Definitions. FRA 2020*. Forest Resources Assessment Working Paper 188. Rome.

Franklin, J. (2010). "Data for species distribution models: the environmental data". In: *Mapping Species Distributions: Spatial Inference and Prediction*. Ecology, Biodiversity and Conservation. Cambridge: Cambridge University Press, pp. 76–104. DOI: 10.1017/CBO9780511810602.008.

Gao, B.-c. (1996). "NDWI—A normalized difference water index for remote sensing of vegetation liquid water from space". In: *Remote Sensing of Environment* 58.3, pp. 257–266. DOI: 10.1016/S0034-4257(96)00067-3.

GDAL/OGR contributors (2021). *GDAL/OGR Geospatial Data Abstraction software Library*. Open Source Geospatial Foundation. URL: https://gdal.org.

Green, D. M. et al. (2020). "Amphibian Population Declines: 30 Years of Progress in Confronting a Complex Problem". In: *Herpetologica* 76.2, pp. 97–100. DOI: 10.1655/0018-0831-76.2.97.

Griffiths, P., C. Nendel, and P. Hostert (2019). "Intra-annual reflectance composites from Sentinel-2 and Landsat for national-scale crop and land cover mapping".

In: *Remote Sensing of Environment* 220, pp. 135–151. DOI: 10.1016/j.rse.2018.10.031.

Guisan, A., W. Thuiller, and N. E. Zimmermann (2017). *Habitat Suitability and Distribution Models. With Applications in R.* Ecology, Biodiversity and Conservation. Cambridge University Press. ISBN: 9781139028271. DOI: 10.1017/9781139028271.

Hall-Beyer, M. (2017). "Practical guidelines for choosing GLCM textures to use in landscape classification tasks over a range of moderate spatial scales". In: *International Journal of Remote Sensing* 38.5, pp. 1312–1338. DOI: 10.1080/01431161.2016.1278314.

Haralick, R. M., K. Shanmugam, and I. Dinstein (1973). "Textural Features for Image Classification". In: *IEEE Transactions on Systems, Man, and Cybernetics* SMC-3.6, pp. 610–621. DOI: 10.1109/TSMC.1973.4309314.

Hastie, T., R. Tibshirani, and J. Friedman (2009). *The Elements of Statistical Learning. Data Mining, Inference, and Prediction.* 2nd ed. Springer Series in Statistics. Springer. ISBN: 978-0-387-84858-7. DOI: 10.1007/b94608.

He, K. S. et al. (2015). "Will remote sensing shape the next generation of species distribution models?" In: *Remote Sensing in Ecology and Conservation* 1.1, pp. 4–18. DOI: 10.1002/rse2.7.

Hendrix, R. et al. (2017). "Differentiation of movement behaviour in an adaptively diverging salamander population". In: *Molecular Ecology* 26.22, pp. 6400–6413. DOI: 10.1111/mec.14345.

Immitzer, M. et al. (2019). "Optimal Input Features for Tree Species Classification in Central Europe Based on Multi-Temporal Sentinel-2 Data". In: *Remote Sensing* 11.22, 2599. DOI: 10.3390/rs11222599.

IUCN (International Union for Conservation of Nature), Conservation International & NatureServe (2009). "Salamandra salamandra". In: *The IUCN Red List of Threatened Species. Version 2021-1.* URL: https://www.iucnredlist.org.

Kiss, I., J. Vörös, and A. Hamer (2021). "Movement patterns within an urban population of fire salamanders highlight the importance of conserving small habitat patches". In: *Journal of Zoology.* DOI: 10.1111/jzo.12949.

Korhonen, L. et al. (2017). "Comparison of Sentinel-2 and Landsat 8 in the estimation of boreal forest canopy cover and leaf area index". In: *Remote Sensing of Environment* 195, pp. 259–274. DOI: 10.1016/j.rse.2017.03.021.

Landesanstalt für Umwelt Baden-Württemberg (LUBW) (2022a). *Meldeplattformen.* URL: https://www.lubw.baden-wuerttemberg.de/natur-und-landschaft/meldeplattformen.

Landesanstalt für Umwelt Baden-Württemberg (LUBW) (2022b). *Projekt LAK - Landesweite Artenkartierung (LAK).* URL: https://www.lubw.baden-wuerttemberg.de/natur-und-landschaft/landesweite-artenkartierung-lak.

Laurin, G. V. et al. (2018). "Above-ground biomass prediction by Sentinel-1 multitemporal data in central Italy with integration of ALOS2 and Sentinel-2 data". In: *Journal of Applied Remote Sensing* 12.1, 016008. DOI: 10.1117/1.JRS.12.016008.

Lemaître, G., F. Nogueira, and C. K. Aridas (2017). "Imbalanced-learn: A Python Toolbox to Tackle the Curse of Imbalanced Datasets in Machine Learning". In: *Journal of Machine Learning Research* 18.17, pp. 1–5. URL: http://jmlr.org/papers/v18/16-365.html.

Lembrechts, J. J., I. Nijs, and J. Lenoir (2019). "Incorporating microclimate into species distribution models". In: *Ecography* 42.7, pp. 1267–1279. DOI: 10.1111/ecog.03947.

Lötters, S. et al. (2020). "The amphibian pathogen *Batrachochytrium salamandrivorans* in the hotspot of its European invasive range: past – present – future". In: *Salamandra. German Journal of Herpetology* 56.3, pp. 173–188. ISSN: 0036-3375.

Manenti, R., E. Lunghi, and G. F. Ficetola (2017). "Cave exploitation by an usual epigean species: a review on the current knowledge on fire salamander breeding in cave". In: *Biogeographia. The Journal of Integrative Biogeography* 32, pp. 31–46. DOI: 10.21426/B632136017.

Martel, A., M. Blooi, et al. (2014). "Recent introduction of a chytrid fungus endangers Western Palearctic salamanders". In: *Science* 346.6209, pp. 630–631. DOI: 10.1126/science.1258268.

Martel, A., A. S.-v. der Sluijs, et al. (2013). "*Batrachochytrium salamandrivorans* sp. nov. causes lethal chytridiomycosis in amphibians". In: *Proceedings of the National Academy of Sciences* 110.38, pp. 15325–15329. DOI: 10.1073/pnas.1307356110.

Martel, A., M. Vila-Escale, et al. (2020). "Integral chain management of wildlife diseases". In: *Conservation Letters* 13.2, e12707. DOI: 10.1111/conl.12707.

Mordelet, F. and J.-P. Vert (2014). "A bagging SVM to learn from positive and unlabeled examples". In: *Pattern Recognition Letters* 37, pp. 201–209. DOI: 10.1016/j.patrec.2013.06.010.

OpenStreetMap Wiki (2021). URL: https://wiki.openstreetmap.org (visited on 10/15/2021).

Pedregosa, F. et al. (2011). "Scikit-learn: Machine Learning in Python". In: *Journal of Machine Learning Research* 12, pp. 2825–2830.

Persson, M., E. Lindberg, and H. Reese (2018). "Tree Species Classification with Multi-Temporal Sentinel-2 Data". In: *Remote Sensing* 10.11, 1794. DOI: 10.3390/rs10111794.

Romero, D., J. Olivero, and R. Real (2012). "Comparative assessment of different methods for using land-cover variables for distribution modelling of *Salamandra*

salamandra longirotris". In: *Environmental Conservation* 40.1, pp. 48–59. DOI: 10.1017/S0376892912000227.

Rouse, J. W. et al. (1974). "Monitoring Vegetation Systems in the Great Plains with ERTS". In: *Proceedings of the Third Earth Resources Technology Satellite-1 Symposium*. NASA SP-351. Vol. 1, pp. 309–317. URL: https://ntrs.nasa.gov/citations/19740022614.

Rufin, P. et al. (2021). "Operational Coregistration of the Sentinel-2A/B Image Archive Using Multitemporal Landsat Spectral Averages". In: *IEEE Geoscience and Remote Sensing Letters* 18.4, pp. 712–716. DOI: 10.1109/LGRS.2020.2982245.

Scheele, B. C. et al. (2019). "Amphibian fungal panzootic causes catastrophic and ongoing loss of biodiversity". In: *Science* 363.6434, pp. 1459–1463. DOI: 10.1126/science.aav0379.

Schmeller, D. S. et al. (2020). "*Batrachochytrium salamandrivorans* kills alpine newts (*Ichthyosaura alpestris*) in southernmost Germany". Correspondence. In: *Salamandra. German Journal of Herpetology* 56.3, pp. 230–232.

Schmidt, B. R., R. Feldmann, and M. Schaub (2005). "Demographic Processes Underlying Population Growth and Decline in *Salamandra salamandra*". In: *Conservation Biology* 19.4, pp. 1149–1156. DOI: 10.1111/j.1523-1739.2005.00164.x.

Schulte, U., D. Küsters, and S. Steinfartz (2007). "A PIT tag based analysis of annual movement patterns of adult fire salamanders (*Salamandra salamandra*) in a Middle European habitat". In: *Amphibia-Reptilia* 28.4, pp. 531–536. DOI: 10.1163/156853807782152543.

Skakun, S. et al. (2017). "Automatic sub-pixel co-registration of Landsat-8 Operational Land Imager and Sentinel-2A Multi-Spectral Instrument images using phase correlation and machine learning based mapping". In: *International Journal of Digital Earth* 10.12, pp. 1253–1269. DOI: 10.1080/17538947.2017.1304586.

Small, D. (2011). "Flattening Gamma: Radiometric Terrain Correction for SAR Imagery". In: *IEEE Transactions on Geoscience and Remote Sensing* 49.8, pp. 3081–3093. DOI: 10.1109/TGRS.2011.2120616.

ESA SNAP (2021). *SNAP - ESA Sentinel Application Platform v8.0.7*. URL: http://step.esa.int.

Spitzen-van der Sluijs, A. et al. (2016). "Expanding Distribution of Lethal Amphibian Fungus *Batrachochytrium salamandrivorans* in Europe". In: *Emerging Infectious Diseases* 22.7, pp. 1286–1288. DOI: 10.3201/eid2207.160109.

Spracklen, B. D. and D. V. Spracklen (2019). "Identifying European Old-Growth Forests using Remote Sensing: A Study in the Ukrainian Carpathians". In: *Forests* 10.2, 127. DOI: 10.3390/f10020127.

Stegen, G. et al. (2017). "Drivers of salamander extirpation mediated by *Batrachochytrium salamandrivorans*". In: *Nature* 544, pp. 353–356. DOI: 10.1038/nature22059.

Steinfartz, S., M. Weitere, and D. Tautz (2007). "Tracing the first step to speciation: ecological and genetic differentiation of a salamander population in a small forest". In: *Molecular Ecology* 16.21, pp. 4550–4561. DOI: 10.1111/j.1365-294X.2007.03490.x.

Stokstad, E. (2014). "The coming salamander plague". In: *Science* 346.6209, pp. 530–531. DOI: 10.1126/science.346.6209.530.

Thein, J. et al. (2020). "Preliminary report on the occurrence of *Batrachochytrium salamandrivorans* in the Steigerwald, Bavaria, Germany". Correspondence. In: *Salamandra. German Journal of Herpetology* 56.3, pp. 227–229.

Thiesmeier, B. and H. Schuhmacher (1990). "Causes of larval drift of the fire salamander, *Salamandra salamandra terrestris*, and its effects on population dynamics". In: *Oecologia* 82.2, pp. 259–263. DOI: 10.1007/BF00323543.

Vasile, G. et al. (2006). "Intensity-Driven Adaptive-Neighborhood Technique for Polarimetric and Interferometric SAR Parameters Estimation". In: *IEEE Transactions on Geoscience and Remote Sensing* 44.6, pp. 1609–1621. DOI: 10.1109/TGRS.2005.864142.

Wagner, N. et al. (2020). "Do habitat preferences of European fire salamander (*Salamandra salamandra*) larvae differ among landscapes? A case study from Western Germany". In: *Salamandra. German Journal of Herpetology* 56.3, pp. 254–264. ISSN: 0036-3375.

Walt, S. van der et al. (June 2014). "scikit-image: image processing in Python". In: *PeerJ* 2, e453. ISSN: 2167-8359. DOI: 10.7717/peerj.453.

Weitere, M. et al. (2004). "Adaptive divergence vs. environmental plasticity: tracing local genetic adaptation of metamorphosis traits in salamanders". In: *Molecular Ecology* 13.6, pp. 1665–1677. DOI: 10.1111/j.1365-294X.2004.02155.x.

Werner, P. et al. (2013). "The role of climate for the range limits of parapatric European land salamanders". In: *Ecography* 36.10, pp. 1127–1137. DOI: 10.1111/j.1600-0587.2013.00242.x.

Appendix A

Table A.1: 5-fold cross-validation statistics for predictor set inclusion.

	AUC		
Predictor Set	Overlap Area	Orbit 65	Orbit 108
Pixel-based classification			
S1	0.806	0.794	0.812
S2	0.907	0.890	0.907
S1 + S2	0.907	0.890	0.909
S1 + S2 + VI	0.908	0.890	0.909
S1 + S2 + Texture	0.909	0.891	0.910
S1 + S2 + Texture + VI	0.91	0.891	0.910
S1 + S2 + Texture + VI + Stream	0.928	0.914	0.932
S1 + S2 + Texture + VI + Stream-Ditch1	0.923	0.909	0.927
S1 + S2 + Texture + VI + Stream-Ditch2	0.923	0.909	0.927
S1 + S2 + Texture + VI + Stream-River	0.929	0.914	0.933
S1 + S2 + Texture + VI + Stream-River-Ditch1	0.924	0.909	0.928
S1 + S2 + Texture + VI + Stream-River-Ditch2	0.924	0.909	0.928
Object-based classification			
S1	0.817	0.800	0.825
S2	0.877	0.863	0.885
S1 + S2	0.878	0.861	0.887
S1 + S2 + VI	0.881	0.864	0.889
S1 + S2 + Texture	0.880	0.862	0.887
S1 + S2 + Texture + VI	0.883	0.865	0.890
S1 + S2 + Texture + VI + Stream	0.898	0.883	0.909
S1 + S2 + Texture + VI + Stream-Ditch1	0.897	0.880	0.907
S1 + S2 + Texture + VI + Stream-Ditch2	0.897	0.880	0.906
S1 + S2 + Texture + VI + Stream-River	0.901	0.884	0.908
S1 + S2 + Texture + VI + Stream-River-Ditch1	0.898	0.881	0.908
S1 + S2 + Texture + VI + Stream-River-Ditch2	0.898	0.881	0.907

S1: Sentinel-1 images; S2: Sentinel-2 bands; VI: vegetation indices.

Series from Lund University

Department of Physical Geography and Ecosystem Science

Master Thesis in Geographical Information Science

1. *Anthony Lawther:* The application of GIS-based binary logistic regression for slope failure susceptibility mapping in the Western Grampian Mountains, Scotland (2008).
2. *Rickard Hansen:* Daily mobility in Grenoble Metropolitan Region, France. Applied GIS methods in time geographical research (2008).
3. *Emil Bayramov:* Environmental monitoring of bio-restoration activities using GIS and Remote Sensing (2009).
4. *Rafael Villarreal Pacheco:* Applications of Geographic Information Systems as an analytical and visualization tool for mass real estate valuation: a case study of Fontibon District, Bogota, Columbia (2009).
5. *Siri Oestreich Waage:* a case study of route solving for oversized transport: The use of GIS functionalities in transport of transformers, as part of maintaining a reliable power infrastructure (2010).
6. *Edgar Pimiento:* Shallow landslide susceptibility – Modelling and validation (2010).
7. *Martina Schäfer:* Near real-time mapping of floodwater mosquito breeding sites using aerial photographs (2010).
8. *August Pieter van Waarden-Nagel:* Land use evaluation to assess the outcome of the programme of rehabilitation measures for the river Rhine in the Netherlands (2010).

9. *Samira Muhammad:* Development and implementation of air quality data mart for Ontario, Canada: A case study of air quality in Ontario using OLAP tool. (2010).

10. *Fredros Oketch Okumu*: Using remotely sensed data to explore spatial and temporal relationships between photosynthetic productivity of vegetation and malaria transmission intensities in selected parts of Africa (2011).

11. *Svajunas Plunge:* Advanced decision support methods for solving diffuse water pollution problems (2011).

12. *Jonathan Higgins:* Monitoring urban growth in greater Lagos: A case study using GIS to monitor the urban growth of Lagos 1990 - 2008 and produce future growth prospects for the city (2011).

13. *Mårten Karlberg:* Mobile Map Client API: Design and Implementation for Android (2011).

14. *Jeanette McBride:* Mapping Chicago area urban tree canopy using color infrared imagery (2011).

15. *Andrew Farina:* Exploring the relationship between land surface temperature and vegetation abundance for urban heat island mitigation in Seville, Spain (2011).

16. *David Kanyari*: Nairobi City Journey Planner: An online and a Mobile Application (2011).

17. *Laura V. Drews:* Multi-criteria GIS analysis for siting of small wind power plants – A case study from Berlin (2012).

18. *Qaisar Nadeem:* Best living neighborhood in the city – A GIS based multi criteria evaluation of ArRiyadh City (2012).

19. *Ahmed Mohamed El Saeid Mustafa:* Development of a photo voltaic building rooftop integration analysis tool for GIS for Dokki District, Cairo, Egypt (2012).

20. *Daniel Patrick Taylor*: Eastern Oyster Aquaculture: Estuarine Remediation via Site Suitability and Spatially Explicit Carrying Capacity Modeling in Virginia's Chesapeake Bay (2013).

21. *Angeleta Oveta Wilson:* A Participatory GIS approach to *unearthing* Manchester's Cultural Heritage '*gold mine'* (2013).

22. *Ola Svensson:* Visibility and Tholos Tombs in the Messenian Landscape: A Comparative Case Study of the Pylian Hinterlands and the Soulima Valley (2013).

23. *Monika Ogden:* Land use impact on water quality in two river systems in South Africa (2013).

24. *Stefan Rova:* A GIS based approach assessing phosphorus load impact on Lake Flaten in Salem, Sweden (2013).

25. *Yann Buhot:* Analysis of the history of landscape changes over a period of 200 years. How can we predict past landscape pattern scenario and the impact on habitat diversity? (2013).

26. *Christina Fotiou:* Evaluating habitat suitability and spectral heterogeneity models to predict weed species presence (2014).

27. *Inese Linuza:* Accuracy Assessment in Glacier Change Analysis (2014).

28. *Agnieszka Griffin:* Domestic energy consumption and social living standards: a GIS analysis within the Greater London Authority area (2014).

29. *Brynja Guðmundsdóttir:* Detection of potential arable land with remote sensing and GIS – A Case Study for Kjósarhreppur (2014).

30. *Oleksandr Nekrasov:* Processing of MODIS Vegetation Indices for analysis of agricultural droughts in the southern Ukraine between the years 2000-2012 (2014).

31. *Sarah Tressel:* Recommendations for a polar Earth science portal in the context of Arctic Spatial Data Infrastructure (2014).

32. *Caroline Gevaert:* Combining Hyperspectral UAV and Multispectral Formosat-2 Imagery for Precision Agriculture Applications (2014).

33. *Salem Jamal-Uddeen:* Using GeoTools to implement the multi-criteria evaluation analysis – weighted linear combination model (2014).

34. *Samanah Seyedi-Shandiz:* Schematic representation of geographical railway network at the Swedish Transport Administration (2014).

35. *Kazi Masel Ullah:* Urban Land-use planning using Geographical Information System and analytical hierarchy process: case study Dhaka City (2014).

36. *Alexia Chang-Wailing Spitteler:* Development of a web application based on MCDA and GIS for the decision support of river and floodplain rehabilitation projects (2014).

37. *Alessandro De Martino:* Geographic accessibility analysis and evaluation of potential changes to the public transportation system in the City of Milan (2014).

38. *Alireza Mollasalehi:* GIS Based Modelling for Fuel Reduction Using Controlled Burn in Australia. Case Study: Logan City, QLD (2015).

39. *Negin A. Sanati:* Chronic Kidney Disease Mortality in Costa Rica; Geographical Distribution, Spatial Analysis and Non-traditional Risk Factors (2015).

40. *Karen McIntyre:* Benthic mapping of the Bluefields Bay fish sanctuary, Jamaica (2015).

41. *Kees van Duijvendijk:* Feasibility of a low-cost weather sensor network for agricultural purposes: A preliminary assessment (2015).

42. *Sebastian Andersson Hylander:* Evaluation of cultural ecosystem services using GIS (2015).

43. *Deborah Bowyer:* Measuring Urban Growth, Urban Form and Accessibility as Indicators of Urban Sprawl in Hamilton, New Zealand (2015).

44. *Stefan Arvidsson:* Relationship between tree species composition and phenology extracted from satellite data in Swedish forests (2015).

45. *Damián Giménez Cruz*: GIS-based optimal localisation of beekeeping in rural Kenya (2016).

46. *Alejandra Narváez Vallejo:* Can the introduction of the topographic indices in LPJ-GUESS improve the spatial representation of environmental variables? (2016).

47. *Anna Lundgren:* Development of a method for mapping the highest coastline in Sweden using breaklines extracted from high resolution digital elevation models (2016).

48. *Oluwatomi Esther Adejoro:* Does location also matter? A spatial analysis of social achievements of young South Australians (2016).

49. *Hristo Dobrev Tomov:* Automated temporal NDVI analysis over the Middle East for the period 1982 - 2010 (2016).

50. *Vincent Muller:* Impact of Security Context on Mobile Clinic Activities A GIS Multi Criteria Evaluation based on an MSF Humanitarian Mission in Cameroon (2016).

51. *Gezahagn Negash Seboka:* Spatial Assessment of NDVI as an Indicator of Desertification in Ethiopia using Remote Sensing and GIS (2016).

52. *Holly Buhler:* Evaluation of Interfacility Medical Transport Journey Times in Southeastern British Columbia. (2016).

53. *Lars Ole Grottenberg*: Assessing the ability to share spatial data between emergency management organisations in the High North (2016).

54. *Sean Grant:* The Right Tree in the Right Place: Using GIS to Maximize the Net Benefits from Urban Forests (2016).

55. *Irshad Jamal:* Multi-Criteria GIS Analysis for School Site Selection in Gorno-Badakhshan Autonomous Oblast, Tajikistan (2016).

56. *Fulgencio Sanmartín:* Wisdom-volkano: A novel tool based on open GIS and time-series visualization to analyse and share volcanic data (2016).

57. *Nezha Acil:* Remote sensing-based monitoring of snow cover dynamics and its influence on vegetation growth in the Middle Atlas Mountains (2016).

58. *Julia Hjalmarsson:* A Weighty Issue: Estimation of Fire Size with Geographically Weighted Logistic Regression (2016).

59. *Mathewos Tamiru Amato:* Using multi-criteria evaluation and GIS for chronic food and nutrition insecurity indicators analysis in Ethiopia (2016).

60. *Karim Alaa El Din Mohamed Soliman El Attar:* Bicycling Suitability in Downtown, Cairo, Egypt (2016).

61. *Gilbert Akol Echelai:* Asset Management: Integrating GIS as a Decision Support Tool in Meter Management in National Water and Sewerage Corporation (2016).

62. *Terje Slinning:* Analytic comparison of multibeam echo soundings (2016).

63. *Gréta Hlín Sveinsdóttir:* GIS-based MCDA for decision support: A framework for wind farm siting in Iceland (2017).

64. *Jonas Sjögren:* Consequences of a flood in Kristianstad, Sweden: A GIS-based analysis of impacts on important societal functions (2017).

65. *Nadine Raska:* 3D geologic subsurface modelling within the Mackenzie Plain, Northwest Territories, Canada (2017).

66. *Panagiotis Symeonidis*: Study of spatial and temporal variation of atmospheric optical parameters and their relation with PM 2.5 concentration over Europe using GIS technologies (2017).

67. *Michaela Bobeck:* A GIS-based Multi-Criteria Decision Analysis of Wind Farm Site Suitability in New South Wales, Australia, from a Sustainable Development Perspective (2017).

68. *Raghdaa Eissa*: Developing a GIS Model for the Assessment of Outdoor Recreational Facilities in New Cities Case Study: Tenth of Ramadan City, Egypt (2017).

69. *Zahra Khais Shahid*: Biofuel plantations and isoprene emissions in Svea and Götaland (2017).

70. *Mirza Amir Liaquat Baig*: Using geographical information systems in epidemiology: Mapping and analyzing occurrence of diarrhea in urban – residential area of Islamabad, Pakistan (2017).

71. *Joakim Jörwall*: Quantitative model of Present and Future well-being in the EU-28: A spatial Multi-Criteria Evaluation of socioeconomic and climatic comfort factors (2017).

72. *Elin Haettner*: Energy Poverty in the Dublin Region: Modelling Geographies of Risk (2017).

73. *Harry Eriksson*: Geochemistry of stream plants and its statistical relations to soil- and bedrock geology, slope directions and till geochemistry. A GIS-analysis of small catchments in northern Sweden (2017).

74. *Daniel Gardevärn:* PPGIS and Public meetings – An evaluation of public participation methods for urban planning (2017).

75. *Kim Friberg:* Sensitivity Analysis and Calibration of Multi Energy Balance Land Surface Model Parameters (2017).

76. *Viktor Svanerud:* Taking the bus to the park? A study of accessibility to green areas in Gothenburg through different modes of transport (2017).

77. *Lisa-Gaye Greene*: Deadly Designs: The Impact of Road Design on Road Crash Patterns along Jamaica's North Coast Highway (2017).

78. *Katarina Jemec Parker*: Spatial and temporal analysis of fecal indicator bacteria concentrations in beach water in San Diego, California (2017).

79. *Angela Kabiru*: An Exploratory Study of Middle Stone Age and Later Stone Age Site Locations in Kenya's Central Rift Valley Using Landscape Analysis: A GIS Approach (2017).

80. *Kristean Björkmann*: Subjective Well-Being and Environment: A GIS-Based Analysis (2018).

81. *Williams Erhunmonmen Ojo*: Measuring spatial accessibility to healthcare for people living with HIV-AIDS in southern Nigeria (2018).

82. *Daniel Assefa*: Developing Data Extraction and Dynamic Data Visualization (Styling) Modules for Web GIS Risk Assessment System (WGRAS). (2018).

83. *Adela Nistora*: Inundation scenarios in a changing climate: assessing potential impacts of sea-level rise on the coast of South-East England (2018).

84. *Marc Seliger*: Thirsty landscapes - Investigating growing irrigation water consumption and potential conservation measures within Utah's largest master-planned community: Daybreak (2018).

85. *Luka Jovičić*: Spatial Data Harmonisation in Regional Context in Accordance with INSPIRE Implementing Rules (2018).

86. *Christina Kourdounouli*: Analysis of Urban Ecosystem Condition Indicators for the Large Urban Zones and City Cores in EU (2018).

87. *Jeremy Azzopardi*: Effect of distance measures and feature representations on distance-based accessibility measures (2018).

88. *Patrick Kabatha*: An open source web GIS tool for analysis and visualization of elephant GPS telemetry data, alongside environmental and anthropogenic variables (2018).

89. *Richard Alphonce Giliba*: Effects of Climate Change on Potential Geographical Distribution of Prunus africana (African cherry) in the Eastern Arc Mountain Forests of Tanzania (2018).

90. *Eiður Kristinn Eiðsson*: Transformation and linking of authoritative multiscale geodata for the Semantic Web: A case study of Swedish national building data sets (2018).

91. *Niamh Harty*: HOP!: a PGIS and citizen science approach to monitoring the condition of upland paths (2018).

92. *José Estuardo Jara Alvear*: Solar photovoltaic potential to complement hydropower in Ecuador: A GIS-based framework of analysis (2018).

93. *Brendan O'Neill*: Multicriteria Site Suitability for Algal Biofuel Production Facilities (2018).

94. *Roman Spataru*: Spatial-temporal GIS analysis in public health – a case study of polio disease (2018).

95. *Alicja Miodońska*: Assessing evolution of ice caps in Suðurland, Iceland, in years 1986 - 2014, using multispectral satellite imagery (2019).

96. *Dennis Lindell Schettini*: A Spatial Analysis of Homicide Crime's Distribution and Association with Deprivation in Stockholm Between 2010-2017 (2019).

97. *Damiano Vesentini*: The Po Delta Biosphere Reserve: Management challenges and priorities deriving from anthropogenic pressure and sea level rise (2019).

98. *Emilie Arnesten*: Impacts of future sea level rise and high water on roads, railways and environmental objects: a GIS analysis of the potential effects of increasing sea levels and highest projected high water in Scania, Sweden (2019).

99. *Syed Muhammad Amir Raza*: Comparison of geospatial support in RDF stores: Evaluation for ICOS Carbon Portal metadata (2019).

100. *Hemin Tofiq*: Investigating the accuracy of Digital Elevation Models from UAV images in areas with low contrast: A sandy beach as a case study (2019).

101. *Evangelos Vafeiadis*: Exploring the distribution of accessibility by public transport using spatial analysis. A case study for retail concentrations and public hospitals in Athens (2019).

102. *Milan Sekulic*: Multi-Criteria GIS modelling for optimal alignment of roadway by-passes in the Tlokweng Planning Area, Botswana (2019).

103. *Ingrid Piirisaar*: A multi-criteria GIS analysis for siting of utility-scale photovoltaic solar plants in county Kilkenny, Ireland (2019).

104. *Nigel Fox*: Plant phenology and climate change: possible effect on the onset of various wild plant species' first flowering day in the UK (2019).

105. *Gunnar Hesch*: Linking conflict events and cropland development in Afghanistan, 2001 to 2011, using MODIS land cover data and Uppsala Conflict Data Programme (2019).

106. *Elijah Njoku*: Analysis of spatial-temporal pattern of Land Surface Temperature (LST) due to NDVI and elevation in Ilorin, Nigeria (2019).

107. *Katalin Bunyevácz*: Development of a GIS methodology to evaluate informal urban green areas for inclusion in a community governance program (2019).

108. *Paul dos Santos*: Automating synthetic trip data generation for an agent-based simulation of urban mobility (2019).

109. *Robert O' Dwyer*: Land cover changes in Southern Sweden from the mid-Holocene to present day: Insights for ecosystem service assessments (2019).

110. *Daniel Klingmyr*: Global scale patterns and trends in tropospheric NO2 concentrations (2019).

111. *Marwa Farouk Elkabbany*: Sea Level Rise Vulnerability Assessment for Abu Dhabi, United Arab Emirates (2019).

112. *Jip Jan van Zoonen*: Aspects of Error Quantification and Evaluation in Digital Elevation Models for Glacier Surfaces (2020).

113. *Georgios Efthymiou*: The use of bicycles in a mid-sized city – benefits and obstacles identified using a questionnaire and GIS (2020).

114. *Haruna Olayiwola Jimoh*: Assessment of Urban Sprawl in MOWE/IBAFO Axis of Ogun State using GIS Capabilities (2020).

115. *Nikolaos Barmpas Zachariadis*: Development of an iOS, Augmented Reality for disaster management (2020).

116. *Ida Storm*: ICOS Atmospheric Stations: Spatial Characterization of CO2 Footprint Areas and Evaluating the Uncertainties of Modelled CO2 Concentrations (2020).

117. *Alon Zuta*: Evaluation of water stress mapping methods in vineyards using airborne thermal imaging (2020).

118. *Marcus Eriksson*: Evaluating structural landscape development in the municipality Upplands-Bro, using landscape metrics indices (2020).

119. *Ane Rahbek Vierø*: Connectivity for Cyclists? A Network Analysis of Copenhagen's Bike Lanes (2020).

120. *Cecilia Baggini*: Changes in habitat suitability for three declining Anatidae species in saltmarshes on the Mersey estuary, North-West England (2020).

121. *Bakrad Balabanian*: Transportation and Its Effect on Student Performance (2020).

122. *Ali Al Farid*: Knowledge and Data Driven Approaches for Hydrocarbon Microseepage Characterizations: An Application of Satellite Remote Sensing (2020).

123. *Bartlomiej Kolodziejczyk*: Distribution Modelling of Gene Drive-Modified Mosquitoes and Their Effects on Wild Populations (2020).

124. *Alexis Cazorla*: Decreasing organic nitrogen concentrations in European water bodies – links to organic carbon trends and land cover (2020).

125. *Kharid Mwakoba*: Remote sensing analysis of land cover/use conditions of community-based wildlife conservation areas in Tanzania (2021).

126. *Chinatsu Endo*: Remote Sensing Based Pre-Season Yellow Rust Early Warning in Oromia, Ethiopia (2021).

127. *Berit Mohr*: Using remote sensing and land abandonment as a proxy for long-term human out-migration. A Case Study: Al-Hassakeh Governorate, Syria (2021).

128. *Kanchana Nirmali Bandaranayake*: Considering future precipitation in delineation locations for water storage systems – Case study Sri Lanka (2021).

129. *Emma Bylund*: Dynamics of net primary production and food availability in the aftermath of the 2004 and 2007 desert locust outbreaks in Niger and Yemen (2021).

130. *Shawn Pace*: Urban infrastructure inundation risk from permanent sea-level rise scenarios in London (UK), Bangkok (Thailand) and Mumbai (India): A comparative analysis (2021).

131. *Oskar Evert Johansson*: The hydrodynamic impacts of Estuarine Oyster reefs, and the application of drone technology to this study (2021).

132. *Pritam Kumarsingh*: A Case Study to develop and test GIS/SDSS methods to assess the production capacity of a Cocoa Site in Trinidad and Tobago (2021).

133. *Muhammad Imran Khan*: Property Tax Mapping and Assessment using GIS (2021).

134. *Domna Kanari*: Mining geosocial data from Flickr to explore tourism patterns: The case study of Athens (2021).

135. *Mona Tykesson Klubien*: Livestock-MRSA in Danish pig farms (2021).

136. *Ove Njøten*: Comparing radar satellites. Use of Sentinel-1 leads to an increase in oil spill alerts in Norwegian waters (2021).

137. *Panagiotis Patrinos*: Change of heating fuel consumption patterns produced by the economic crisis in Greece (2021).

138. *Lukasz Langowski*: Assessing the suitability of using Sentinel-1A SAR multi-temporal imagery to detect fallow periods between rice crops (2021).

139. *Jonas Tillman*: Perception accuracy and user acceptance of legend designs for opacity data mapping in GIS (2022).

140. *Gabriela Olekszyk*: ALS (Airborne LIDAR) accuracy: Can potential low data quality of ground points be modelled/detected? Case study of 2016 LIDAR capture over Auckland, New Zealand (2022).

141. *Luke Aspland*: Weights of Evidence Predictive Modelling in Archaeology (2022).

142. *Luís Fareleira Gomes*: The influence of climate, population density, tree species and land cover on fire pattern in mainland Portugal (2022).

143. *Andreas Eriksson*: Mapping Fire Salamander (*Salamandra salamandra*) Habitat Suitability in Baden-Württemberg with Multi-Temporal Sentinel-1 and Sentinel-2 Imagery (2022).